UNIVERSITY OF
LINCOLN

AN INVESTIGATION INTO COMBINING BOTH FACIAL DETECTION AND LANDMARK LOCALISATION INTO A UNIFIED PROCEDURE USING GPU COMPUTING

J M McDonagh

MSc by Research

2016

AN INVESTIGATION INTO COMBINING BOTH FACIAL DETECTION AND LANDMARK LOCALISATION INTO A UNIFIED PROCEDURE USING GPU COMPUTING

Acknowledgements

Many thanks to my supervisor Georgios Tzimiropoulos for your guidance and support throughout the course of this project.

Abstract

This thesis describes the design and implementation of a unified framework for face detection and landmark alignment in arbitrary in the wild images. Traditionally, both of these problems have been addressed separately in literature with impressive results being recently reported in both of these fields. But, if one was to construct a pipeline consisting of a state-of-the-art face detection method followed by a state-of-the-art facial landmark localisation algorithm, the overall performance outcome would not be proficient enough to be used in high level algorithms such as face recognition and facial expression. This is because the accuracy produced by the face detector is not sufficiently high enough to initialise the landmark localisation algorithm.

To address this aforementioned limitation, this thesis aims to propose an approach that combines both of these tasks into a single unified algorithm that can be run in real time, by utilising the parallel computing architecture of the graphics processing unit (GPU). This will be done by using a Cascaded-Regression (CR) algorithm in a sliding window fashion. The proposed system will exploit the CR algorithms ability to compute the 2D pose of a face from rough initial estimates, in order to generate a Hough-Transform voting scheme for detecting candidate faces and filtering out irrelevant background. The obtained detection surface will then be further refined using SVM to yield both face detections and the location of their parts.

The proposed system for this thesis will be built within the MATLAB environment, using a MEX-file which will provide an interface to the proposed CUDA algorithm. The results of which, will be tested against current state-of-the-art methods for both face detection and landmark localisation.

We evaluate performance on the most widely used data sets in face detection, namely annotated faces in-the-wild (AFW) (Zhu and Ramanan, 2012), Face Detection Dataset and Benchmark (FDDB) (Jain and Learned-Miller, 2010) and Caltech Occluded Faces in the Wild (COFW) (Burgos-Artizzu, Perona and Dollár, 2013). The empirical results demonstrate that the proposed unified framework achieves state-of-the-art performance in both face detection and facial alignment, and that our detector clearly outperforms all commercial and published methods by a margin of over 10% in detection accuracy on the AFW dataset.

Table of Contents

1 Introduction 1

1.1 Aims 4

2 Related Work 6

2.1 Face Detection 6

2.2 Facial landmark localisation 8

3 SIFT 11

3.1 Keypoint Descriptor 11

4 Deformable Global Consensus Model 14

4.1 Shape model and appearance 14

4.1.1 Shape model 14

4.1.2 Appearance 17

4.2 Deformable model fitting with PO-CR 18

4.3 Training 22

4.4 Hough-Transform Voting 22

4.5 Final re-scoring 23

4.6 Complexity 23

5 CUDA 24

5.1 CUDA architecture 24

5.1.1 Streaming multiprocessor (SMX) 25

5.2 Compute Capability 26

5.3 Kernel Functions 26

5.4 Thread hierarchy 27

5.4.1 Thread Blocks 28

5.4.2 Threads 29

5.5 Memory Hierarchy 29

6 Implementation 32

6.1 DGCM 34
6.1.1 Memory allocation 34
6.1.2 SIFT 34
6.1.3 PO-CR 35
6.1.4 CUDA Vector-Matrix multiplication 36
6.1.5 Voting 38
6.2 Support Vector Machine (SVM) 42
6.2.1 Feature normalisation 43
6.2.2 Cross-validation 43
6.2.3 Training 44
6.2.4 Classification 44
7 Results 46
7.1 Performance measures 46
7.2 Face detection 47
7.2.1 Annotated faces in-the-wild 47
7.2.2 Face Detection Dataset and Benchmark 49
7.3 Landmark localisation 50
7.4 Execution times 52
7.5 Images 53
7.5.1 AFW 53
7.5.2 FDDB 55
7.5.3 COFW 58
8 Conclusion 60
9 Reference 61
10 Appendix A 67
10.1 CUDA and OpenCL Performance comparison 68
10.2 Conclusion 73

List of Figures

Figure 1.1: Wales, International Rugby team (selfie) (source: Wales Online, 2015) .. 1
Figure 1.2: An example of face detection using the Deformable Part Model (DPM) (Mathias et al, 2014). Using the PASCAL VOC protocol of 50% overlap (Everingham, et al., 2009), we can see that the woman on the left, although detected, does not pass the standard detection protocol. Red bounding boxes are the ground truth, yellow boxes are detected faces and green boxes are false positives. 2
Figure 1.3: An example of face detection using the proposed system. Both faces are not only fully detected, but are also nearly identical to the ground truth bounding boxes. Red bounding boxes are the ground truth, yellow boxes are detected faces and green boxes are false positives. 3
Figure 1.4: Examples of detected faces from the AFW dataset using the standard PASCAL VOC protocol of 50% overlap. Red bounding boxes are the ground truth and yellow boxes are detected faces. 4
Figure 3.1: For each 4x4 sub-region, the gradient magnitudes are weighted with the Gaussian filter (blue circle), the result of which is then added to the corresponding bin of the sub-region histogram that matches the gradient orientation. (Source: Gil, 2013) 12
Figure 4.1: Examples of annotated landmarks for both frontal and profile faces from the Helen and ALFW datasets 15
Figure 4.2: frontal and profile mean shapes 16
Figure 4.3: Statistical distribution of facial feature points. The black dots represent 600 facial shapes that have been normalised by Procrustes analysis. The red dots signify the mean shape. (Wang et.al, 2014) 17
Figure 4.4: Example of a face warped to the mean shape. The left image is the source image taken from a training set with the landmarks triangulated using Delaunay triangulation, the pixels within each triangle are then warped to the corresponding triangle in the mean shape. This gives us the shape-free texture, which is shown in the right image 18

Figure 4.5: Overview of the proposed Deformable Global Consensus Model. For each iteration, if the current threshold is above zero, Hough-Transform voting is used to reject any shapes peaks below the threshold. 21
Figure 5.1: Kepler GK110 Full chip block diagram (Source: NVIDIA, 2012, p6)....... 24
Figure 5.2: SMX: 192 single-precision CUDA cores, 64 double-precision units, 32 special function units (SFU), and 32 load/store units (Source: NVIDIA, 2012, p8)... 25
Figure 5.3: Thread hierarchy in the CUDA programming model. (Source: NVIDIA, developer zone, 2015).. 28
Figure 5.4: Kepler's memory hierarchy (Source: NVIDIA, 2012, p13) 30
Figure 6.1: System overview, the red outlined boxes are the Mex functions that are used to provide an interface to CUDA C++ 32
Figure 6.2: 2D matrix allocation. When allocating device memory via the cudaMallocPitch function call, rows are padded (yellow blocks) to guarantee that the beginning of each row begins on a 128 memory boundary. 34
Figure 6.3: Warp reduction using shuffle down, for illustrative purposes this figure only shows a half warp (16 lanes). The first parameter of the __shfl_down intrinsic is the register to return, the second is the offset from the calling lane of the warp and the third parameter is the width of the warp segment which must be of size 2, 4, 8, 16, or 32. The default size is 32. 37
Figure 6.4: Original image from the AFW dataset 38
Figure 6.5: Hough-Transform voting surface after first iteration 39
Figure 6.6: Hough-Transform voting surface after second iteration 39
Figure 6.7: Hough-Transform voting surface after fifth iteration 39
Figure 6.8: Hough-Transform voting surface after tenth iteration 40
Figure 6.9: Hough-Transform voting surface after fifteenth iteration 40
Figure 6.10: SVM scores generated for candidate faces..................... 40
Figure 6.11: Final fitted results after threshold has been applied 41
Figure 6.13: Stream compaction. Any vote score (yellow boxes) with a value equal or less than one is set to minus one in the index array, then the function copy_if from the thrust library is used to compact the array. 41
Figure 6.14: Optimal separating hyperplane, the three filled in shapes are the support vectors (Source: OpenCV, 2016) 42
Figure 7.1: Precision-Recall curve of different evaluation methods on the AFW dataset. With Intersection-over-Union (IoU) overlap set to 50%..................... 48

Figure 7.2: Precision-Recall curve of different evaluation methods on the AFW dataset. With Intersection-over-Union (IoU) overlap set to 75%............................... 48
Figure 7.3: FDDB Discrete scores.. 49
Figure 7.4: FDDB Continuous scores (true positive ratio is IoU between detection ellipse and ground-truth ellipse.) 50
Figure 7.5: Accumulated point-to-point error, relative to size of face, for 474 annotated faces from the AFW dataset... 51
Figure 7.6: Accumulated point-to-point error, relative to size of face, for 507 annotated faces from the COFW dataset.. 51
Figure 8.1: FDDB dataset. Example of low resolution missed faces. Yellow ellipses show faces that are detected, and red ellipses show faces that are not detected.... 60
Figure 10.1: Unified performance comparison of selected benchmarks using NVIDIA’s GeForce GTX 280 and GTX480. It is assumed that CUDA and OpenCL have a similar performance if the result lies between 0.9 and 1.1 (Source: fang et al, 2011).. 70
Figure 10.2: Initial benchmarks for CUDA and OpenCL, running near identical kernel code on an NVIDIA Tesla C1060 GPU. (Source: Komatsu et al. 2010) 72
Figure 10.3: Performance of benchmarks after applying manual optimisations. (Source: Komatsu et al. 2010)... 72

List of Tables

Table 5.1: CUDA Compute Capability 26

Table 7.1: Scaling factors and resulting grid dimensions of a VGA image, with execution times for frontal, right profile and left profile models measured in milliseconds 52

Table 10.1: Discrete graphics chip market share 2015 (Source: Jon Peddie Research, 2015) 67

Table 10.2: CUDA and OpenCL GPU kernel execution, data transfer and application running costs. All times are measured in seconds (Source: Karimi et al, 2010). 69

Table 10.3: CUDA and OpenCL execution times for a tiled 3D-FWT implementation on an input video containing 64 frames of increasing sizes. All times are measured in milliseconds. (Source: Bernabé et al, 2012). 71

1 Introduction

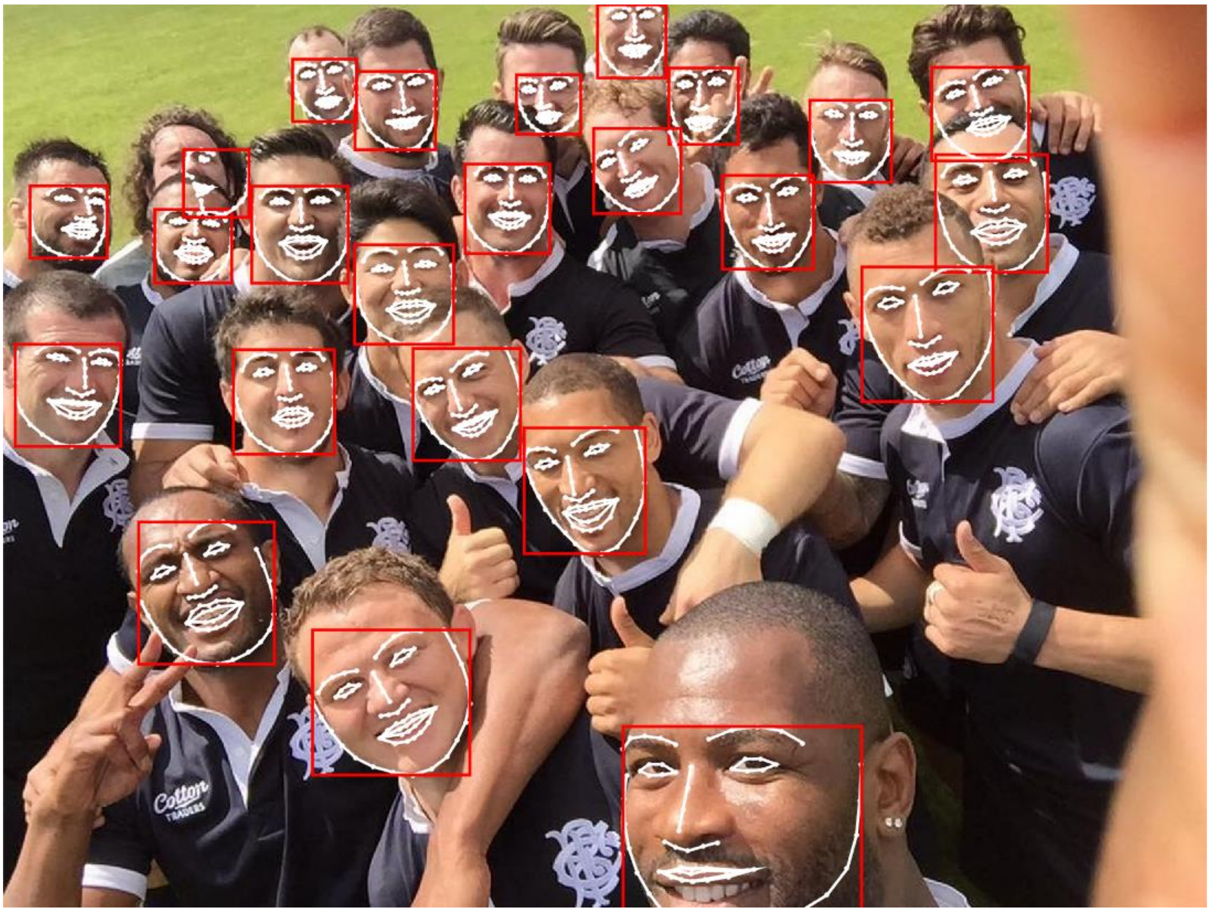

Figure 1.1: Wales, International Rugby team (selfie) (source: Wales Online, 2015)

Among all computer vision research topics, the field of human facial image processing is one of the most challenging. It covers such a vast area of research that it can be broken down into multiple sub-topics such as face detection, recognition, tracking, pose estimation, landmark localisation, expression analysis and animation. Much of this research has made its way into the modern day consumer market: digital cameras for instance use face detection to locate a face or faces in the viewfinder and then fine tune the focus and exposure to give the best possible picture. Digital cameras can also use expression analysis to detect if a person is smiling, and if so the camera will automatically take a picture.

Facial detection can be described as finding the location and size of a face or multiple faces within an arbitrary image, in Figure 1.1 the red bounding boxes show the detected faces. Facial landmark localisation can be described as finding the exact location of facial features, such as eyes, lips, nose, jawline etc., in Figure 1.1 these are shown as the white facial shapes.

Facial detection and landmark localisation are both non-trivial problems. This is due to the human face being a highly variable, deformable object that can vary drastically from image to image, due to pose (scale, rotation and translation), expression, identity, occlusion and illumination. Research into solving both detection and localisation has traditionally been approached as two separate problems with numerous research papers in each field reporting extremely good results for very challenging in-the-wild images. However, for many subsequent, higher level tasks, like face recognition, facial expression and attribute analysis, what matters most is the overall performance in terms of accuracy in landmark localisation. Notably, recent state-of-the-art methods for such tasks rely heavily on the accurate detection of facial landmarks, see for example Chew, et al. (2012) and Chen, et al. (2013).

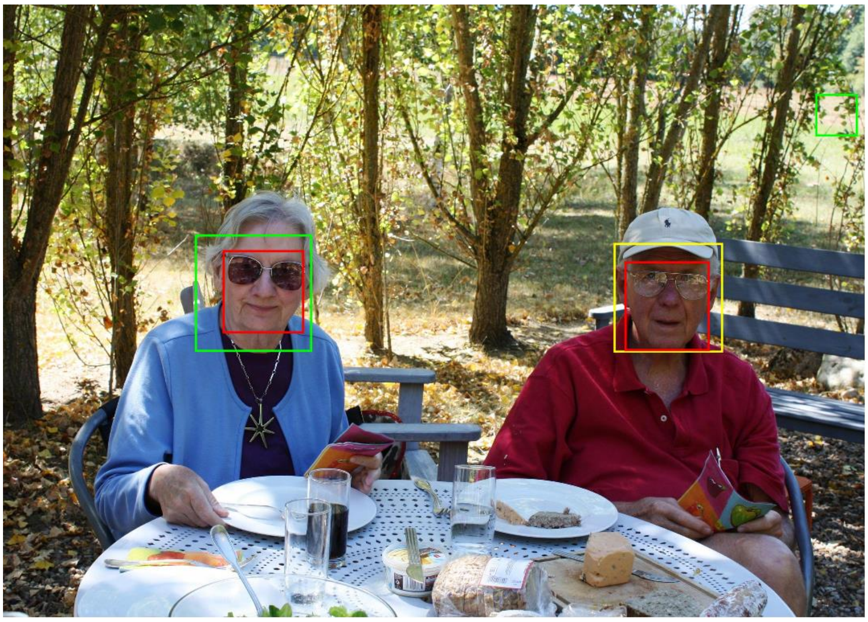

Figure 1.2: An example of face detection using the Deformable Part Model (DPM) (Mathias et al, 2014). Using the PASCAL VOC protocol of 50% overlap (Everingham, et al., 2009), we can see that the woman on the left, although detected, does not pass the standard detection protocol. Red bounding boxes are the ground truth, yellow boxes are detected faces and green boxes are false positives.

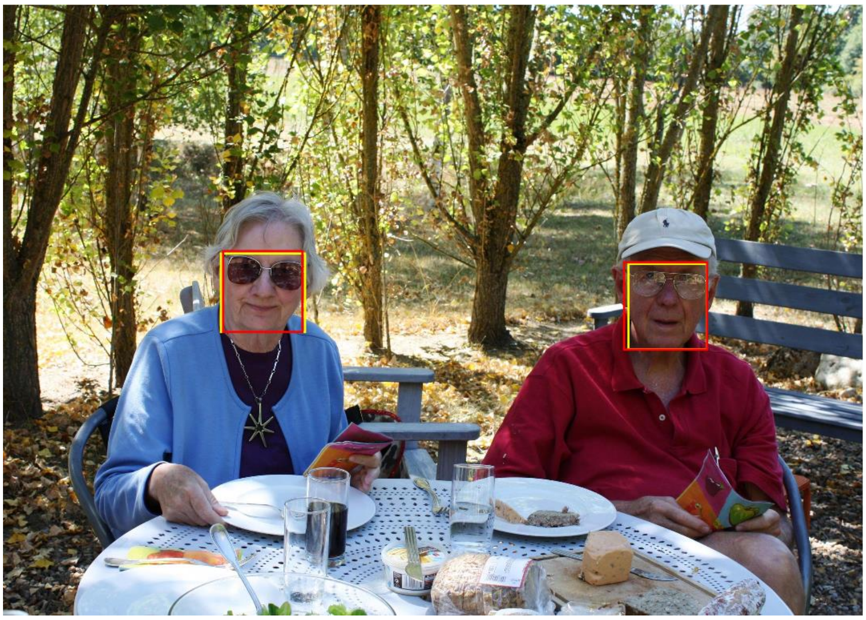

Figure 1.3: An example of face detection using the proposed system. Both faces are not only fully detected, but are also nearly identical to the ground truth bounding boxes. Red bounding boxes are the ground truth, yellow boxes are detected faces and green boxes are false positives.

The problem with using the traditional pipeline of first detecting an unseen face in an image and then using its detected bounding box to initialise a landmark localisation algorithm is twofold: first the land mark localisation algorithm needs to be trained to a specific face detector, so therefore, if the detector is changed at any point in time, then the localisation algorithm will also need to be retrained. Secondly, although current state of the art detectors can find faces in an arbitrary image with a high degree of accuracy as illustrated in Figure 1.2, the reality is the detected bounding boxes that are generated do not fit the faces perfectly. This inaccuracy means that the starting positions and scales that are obtained from these detected bounding boxes is insufficient for initialising a facial localisation algorithm. The reason for this is that facial detectors follow the PASCAL VOC precision-recall protocol for object detection, where in order for an object to be detected it only needs to have a 50% overlap between the ground truth and the predicted bounding box. Although it can be argued that this problem can be mitigated by running multiple initialisations of the landmark localisation algorithm, it is unclear how to select and/or combine the best fittings in a principled manner.

The aim of this thesis is to address this aforementioned limitation by producing a unified solution that jointly addresses both facial detection and landmark detection while at the same time producing a high degree of accuracy in landmark localisation. The proposed approach that is used in this thesis is largely motivated by the efficiency and robustness of recent Cascaded Regression (CR) approaches in facial landmark localisation. Instead of using a face detector to initialise them, the system that is proposed in this thesis, will instead, employ them in a sliding window fashion, in order to detect the location of all faces in an image.

This will be accomplished in real time by utilising the parallel computing architecture of the graphics processing unit (GPU), and the implementation will be based on using NVIDIAs Compute Unified Device Architecture (CUDA). The proposed system will be built within the MATLAB environment, using a MEX-file that will provide the interface to CUDA. The results of which, will be tested against current state-of-the-art methods for both face detection and landmark localisation.

1.1 Aims

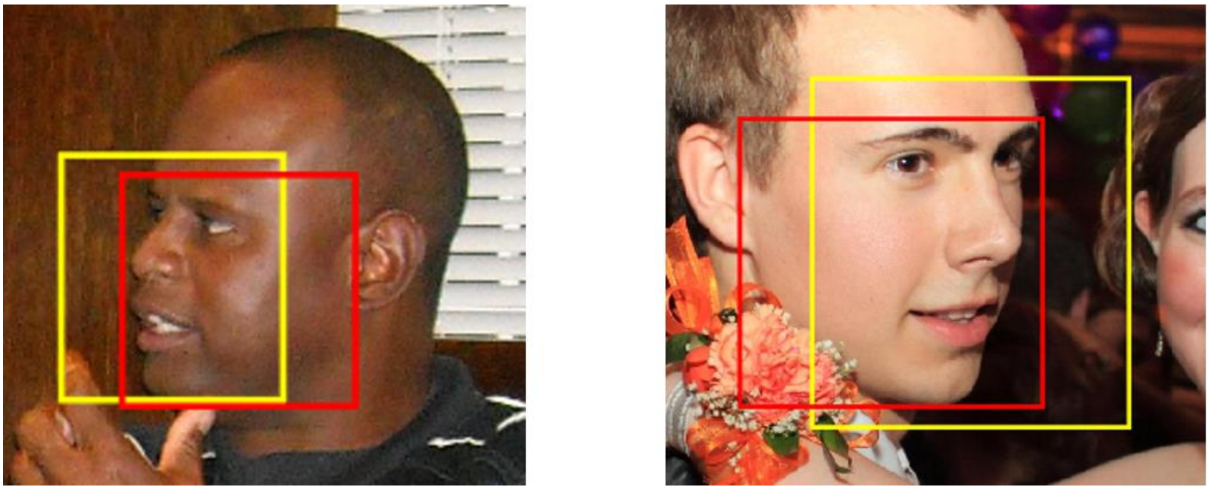

Figure 1.4: Examples of detected faces from the AFW dataset using the standard PASCAL VOC protocol of 50% overlap. Red bounding boxes are the ground truth and yellow boxes are detected faces.

As can be seen from Figure 1.4 having an overlap threshold of 50% to detect a face can produce a wide degree of inaccuracy in the actual detection of a face. The aim of this thesis is to propose a unified solution that jointly addresses both facial detection and landmark detection to not just find faces in an arbitrary image but to detect them with a high degree of accuracy. This will be achieved by exploiting the ability of the Cascaded-Regression algorithm PO-CR (Tzimiropoulos, 2015) to compute the 2D pose of a face from rough initial estimates over a grid which covers the entire image, to generate peaks via a Hough-transform voting scheme to find the position of faces in an image. Thereby if a face is detected, it will be able to generate a bounding box from the final pose estimation, that is close to the ground truth bounding box.

2 Related Work

2.1 Face Detection

Ever since the ground-breaking work of Viola and Jones (2004), the topic of face detection has become one of the most actively researched areas within the computer vision community. The results of their work can also be seen in many of today's high-tech commercial gadgets, such as digital cameras and smartphones.

The objective of face detection is to localise and determine the scales of all faces that are contained within an arbitrary image. This is not a trivial problem to solve, due to variations in pose, illumination, expression and occlusion. In recent years a multitude of different methodologies into the problem of solving multi-view face detection have been proposed, which have reported a varying degree of success. These methodologies can be summarised into three distinct groups, cascade, deformable part models (DPM) and Neural Networks.

The Viola and Jones (2001) detector, which is also called the detector cascade, made it possible to rapidly detect up-right faces in real-time with very low computational complexity. Their detector was successful because of three reasons: firstly, they represented grey scale images in a structure which they called the integral image; this allowed Haar-like features to be calculated extremely fast. Secondly, simple classifiers where generated by selecting a small number of critical features from a larger set of potential features using the adaptive boosting algorithm (AdaBoost) (Freund and Schapire, 1995). Finally, to improve the speed of the detector, each search window is initially checked against a simple classifier, if the search window passes that stages threshold value, it would then become subject to more rigorous testing against more complex classifiers. This threshold culling is repeated at each stage in the cascade, enabling background regions in the image to be discarded as quickly as possible, with little computation.

While Viola and Jones (2001) detector could accurately find up-right faces of any scale in an arbitrary image, they often failed to detect faces with arbitrary poses or that were partially occluded. To address the issue of non-upright and non-frontal faces, Viola and Jones (2003) proposed a two stage approach, which first estimates the pose of the face with the use of a decision tree, and then uses the corresponding cascade detector that is trained on that pose. The problem with using this method is that any errors made while evaluating the pose in the decision tree are irreversible.

Instead of making an exclusive selection of the path for a sample, Huang, et al. (2005) multi-view vector boosting algorithm used a width first search (WFS) tree structure, where each branching node computes a vector, this allowed the sample to be passed into multiple children. By using this soft branching technique, the risk of misclassification is greatly reduced compared to Viola and Jones (2003) decision tree method. Huang, et al. (2005) multi-view face detector covers an in-plane rotation of $\pm$45 degrees. To make it rotation invariant they simply constructed 3 more detectors at 90, 180 and 270 degrees.

Most of the recent research into face detectors is based on the DPM structure which was originally proposed by (Felzenszwalb, et al., 2008), where a face is defined as a collection of parts. These parts are defined via unsupervised or supervised training, and a classifier, the so-called latent SVM, is trained to find those parts and their geometric relationship. They are usually fine-tuned to work efficiently with Histogram of Orientation (HOG) features.

A unified approach to face detection, pose estimation and landmark (eyes, eyebrows, nose mount and jaw line) localisation using the DPM framework was proposed by (Zhu and Ramanan, 2012). Their approach defined a part at each facial landmark and used a mixture of tree based structure models to capture the topological changes due to varying viewpoints.

DMP detectors are robust to partial occlusion because they can detect faces even when some of the parts are not present. A notable extension to (Zhu and Ramanan, 2012) which handles occlusion of parts in a more robust way was suggested by (Ghiasi and Fowlkes, 2014) where they describe a hierarchical DPM for face detection and landmark localisation that explicitly models likely patterns of occlusion and improves landmark localisation. Their model can also predict which landmarks are occluded.

Mathias, et al. (2014) reported in their paper that a properly tuned vanilla DPM face detector performs comparably with a multi-channel, multi-view version of the Viola-Jones detector, and that they both produce state-of-the-art performance on both the FDDB and AFW data sets. Therefore, it can be argued that part based approaches are not always superior to standard approaches based on multi-view rigid templates, especially when a large amount of training data is available.

Observing that aligned face shapes provide better features for face classification, (Chen, et al., 2014) proposed to combine face detection and alignment into the same cascade framework by learning a classifier at each stage, not only on the image, but also on the previous stages estimated shape, in what is called shape-indexed features.

Chen, et al. (2014) along with Mathias, et al. (2014) are the current state of-the-art in face detection.

2.2 Facial landmark localisation

Finding facial landmarks such as eyes, nose, mouth and chin in arbitrary images is not a trivial task. This is due to the subjective morphology of the human face. Human faces, even of the same person can vary enormously from image to image, due to pose, illumination, occlusion and expression. The human face is typically modelled as a deformable object that can vary in terms of shape and appearance. Having accurate facial alignment is essential for many higher level applications such as face recognition, tracking, animation and expression analysis.

In computer vision there has been a long history in the field of face alignment, where numerous approaches such as Active Shape Models (ASM) (Cootes & Taylor, 1992), Active Appearance Models (AAM) (Cootes & Taylor, 1992; Cootes, et al., 2001; Matthews and Barker, 2004), Constrained Local Models (CLM) (Cristinacce and Cootes, 2006; Saragih, et al., 2011) and most recently cascaded regression-based techniques (CR) have been proposed to solve this conundrum, with varying degrees of success (Dollar, et al., 2010; Cao, et al., 2012; Tzimiropoulos, 2015).

One of the earliest works in facial alignment was the ASM which was originally proposed by (Cootes & Taylor, 1992). ASMs use a point distribution model (PDM) to capture the variations in shape from a training set of images. The PDM is learned off-line by first applying Procrustes analysis and then Principle Component Analysis (PCA).

A natural successor to ASMs was the AAM which was first suggested by (Cootes, et al., 1998). AAMs try to solve the problem of face alignment by capturing the combined statistical variations of both shape and texture into a single appearance model using linear regression. A more optimised approach of matching statistical models of appearance to images was proposed by (Cootes, et al., 2001), which replaced the linear regression model with a more simplified Gauss-Newton gradient descent procedure. They assumed that because the Jacobian matrix was being computed in a normalised reference frame, it could be considered approximately fixed and thus could be pre-calculated by numerical differentiation from the training set. This was later showed to perform badly, both in terms of the number of iterations required to converge and in the accuracy of the final fit (Matthews and Barker, 2004).

To avoid the resulting inefficiencies in convergence and robustness during fitting, the inverse compositional algorithm (ICA) was proposed by (Matthews and Barker, 2004). But, unlike the previous AAMs that jointly built generative models of both texture and shape, ICA treated the variations of shape and appearance independently. ICA is based on a variation of the Lucas-Kanade (LK) image alignment algorithm (Lucas and Kanade, 1981), which is a Gauss-Newton gradient descent non-linear optimisation algorithm.

The problem with the LK algorithm is that it is extremely computationally intensive. The reason for this is, because the appearance parameters vary with each iteration and hence the Jacobian, the Hessian and its inverse need to also be recalculated. ICA solves this problem by reversing the roles of the reference and template images, as suggested by (Hager and Belhumeur, 1998), therefore making it possible to pre-calculate the Jacobian and the inverse Hessian matrix. Because ICA reverses the roles of the reference and template images, the update parameters need to be inverted before they are composed with the current estimate of the warp parameters. This lead to a very efficient fitting algorithm, which achieved faster convergence and enhanced convergence properties compared to previous AAMs.

However, this was later shown to not work very well on unseen images, because the learned appearance model had limited expressive power in capturing variations in pose, expression, and illumination (Cristinacce and Cootes, 2006). AAMs were also shown to be very sensitive to initialisation because of the gradient descent optimisation. (Asthana, et al., 2009)

Because of the inability of AAMs to generalise well to unseen images, recent research has been in the use of CLMs which was introduced by (Cristinacce and Cootes, 2006).

CLMs are based on ASMs, and use a similar appearance model to AAMs, but instead of trying to approximate the image pixels directly, they sample texture patches around the individual feature points. CLMs have been shown to be more robust to occlusion and illumination compared to AAMs, and they also outperform AAMs in terms of landmark accuracy. A notable extension to CLM is in the seminal work of (Saragih, et al., 2011), where they proposed a framework for deformable model fitting, known as the Regularized Landmark Mean-Shift (RLMS), which has shown state-of-the-art results under uncontrolled natural settings.

The proposed system in this thesis uses cascade regression (CR) to fit a deformable template to each sub-window in a given image. CR is based on Cascade pose regression (CPR) which was originally proposed by (Dollar, Welinder and Perona, 2010). CPR is an iterative regression method that uses the pose estimation from the previous regressor in the cascade to calculate the new shape-index features, which are to be used as input to the current regressor. Starting from the mean shape the pose estimation is gradually refined with each step in the cascade. CPR has been shown to produce exceptional results on a variety of tasks and, owing to its efficiency and accuracy, it has recently been the focus of investigation by numerous authors for the problem of face alignment.

The idea of using CPR within the field of face alignment was first explored by (Cao, et al., 2012) where they used Explicit Shape Regression (ESR) for facial alignment. Their approach produced exceptional results in terms of both accuracy and efficiency on the Labelled Face Parts in the Wild (LFPW) data set (Belhumeur, et al., 2011).

Project-Out Cascaded Regression (PO-CR) proposed by (Tzimiropoulos, 2015) uses regression to learn and employ a sequence of averaged Jacobian and Hessian matrices, one for each iteration, in a subspace orthogonal to the facial appearance variation. PO-CR has been shown to produce state-of-the-art performance on multiple facial databases.

The proposed system in this thesis uses PO-CR to fit a deformable model. However, the aim of this thesis is not face alignment given a face detection initialisation, but joint face and facial landmark detection.

3 SIFT

Scale Invariant Feature Transform (SIFT) is an approach for detecting and extracting local feature descriptors that are invariant to changes in scale and rotation and partially invariant to changes in illumination, noise, 3D viewpoint and affine transformations (skew, perspective distortion). SIFT was developed by (Lowe, 2004) and is a continuation of his previous work on invariant feature detection (Lowe, 1999). SIFT is also patented by the University of British Columbia.

SIFT can be broken down into four main stages:

1. Identifying locations of peaks (minima / maxima) in scale space
2. Keypoint localisation
3. Orientation assignment
4. Keypoint descriptor

In our implementation of the SIFT descriptor, the keypoint scale and rotation are not needed, and the location of the keypoints are predefined. Therefore, in the next section we will just describe Lowe's (2004) keypoint descriptor.

3.1 Keypoint Descriptor

The SIFT descriptor can be described as a 3D spatial histogram of the orientation of the gradients in a local neighbourhood around an interest point (keypoint).

The gradient magnitude $m(x, y)$, and gradient orientation $\theta(x, y)$, for all points in the selected image $L(x, y)$ are computed by using pixel differences

$$m(x, y) = \sqrt{\big(L(x+1, y) - L(x-1, y)\big)^2 + \big(L(x, y+1) - L(x, y-1)\big)^2} \quad (3.1)$$

$$\theta(x, y) = \tan^{-1}\Big(\big(L(x, y+1) - L(x, y-1)\big) / \big(L(x+1, y) - L(x-1, y)\big)\Big) \quad (3.2)$$

The gradient magnitude measures the steepness of slope at each pixel in an image, for example if the magnitude is a high value it shows that there is a big change, whereas a low value means there is little to no change. The gradient orientation is the angle made by the normal vector to the gradient surface in the direction of increasing change and is measured in radians.

The gradient magnitudes, Equation (3.1) and orientations, Equation (3.2) are sampled in a neighbourhood around the keypoint location on the selected image. Each sample that is added to the histogram is weighted by its gradient magnitude multiplied by a circular Gaussian kernel with a standard deviation equal to half the width of the descriptor window. Lowe (2004) states that the purpose of the Gaussian window is to avoid sudden changes in the descriptor with small changes in the position of the window, and to give less emphasis to gradients that are far from the centre of the descriptor, as these are most affected by misregistration errors.

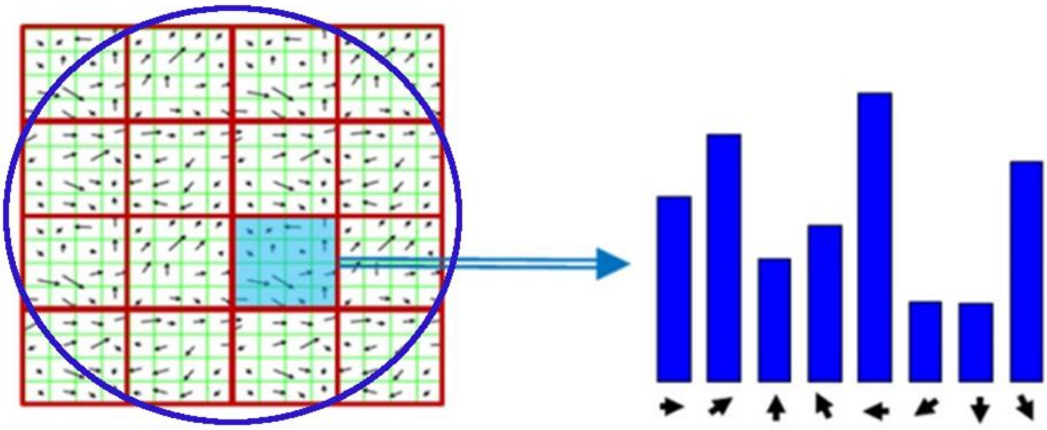

Figure 3.1: For each 4x4 sub-region, the gradient magnitudes are weighted with the Gaussian filter (blue circle), the result of which is then added to the corresponding bin of the sub-region histogram that matches the gradient orientation. (Source: Gil, 2013)

Lowe (2004) uses a 16x16 local neighbourhood centred on a keypoint that is split into 4x4 sub-regions of 16 pixels each, Figure 3.1. Each sub-region is characterised by its gradient contributions to an 8 bin orientation histogram, where each bin covers a 45-degree range, giving a total of 360 degrees. The histogram can be sensitive to noise if the orientation values are close to the boundaries of a bin, therefore to solve this Lowe (2004) uses trilinear interpolation to distribute the value over two adjacent bins. Finally, the 16 orientation histograms are concatenated to produce the 128 element descriptor vector (16 sub-regions x 8 orientation bins).

To make the descriptor invariant to affine changes in illumination the vector is normalised to unit length. Lowe (2004) also thresholds the values of the normalised vector so that no value is above 0.2 and then re-normalises the vector. This is done to reduce the influence of large gradient magnitudes and therefore put more emphasis onto the distribution of gradient orientations.

4 Deformable Global Consensus Model

The propose system scans an image in a sliding window fashion and for each candidate location it fits a generative facial deformable model using the current state-of-the-art Project-Out Cascaded-Regression (PO-CR) algorithm which was proposed by (Tzimiropoulos, 2015). Image locations that converge to the same location cast votes for that location in a fashion similar to that of Hough Transform. After thresholding the surface of votes, and performing non-maximal suppression (NMS) to remove all the low scoring detections that refer to the same face, we end up with only a few candidate locations per image. Next we calculate the median shape of the candidate locations to produce a single fitted shape. Finally, the support vector machine (SVM) scores are calculated by extracting both the Scale-Invariant Feature Transform (SIFT) and colour features from around the landmarks of each of the fitted shapes.

The main components of the proposed Deformable Global Consensus Model (DGCM) are analysed as follows.

4.1 Shape model and appearance

DGCM uses Cascaded Regression (CR) to fit a deformable template to each sub-window of a given image. The CR method that is used for this purpose is the recently proposed PO-CR which has been shown to produce excellent fitting results for faces with very large pose and expression variation. PO-CR uses parametric shape and appearance models both learned with Principal component analysis (PCA).

4.1.1 Shape model

The shape model is first obtained by annotating a set of landmarks that are placed at pre-defined locations which best describe the face. This is repeated over a set of training facial images. Figure 4.1 shows examples of frontal and profile annotated landmarks on various human faces.

Annonatated frontal faces from Helen training set

Annonatated profile faces from ALFW

Figure 4.1: Examples of annotated landmarks for both frontal and profile faces from the Helen and ALFW datasets

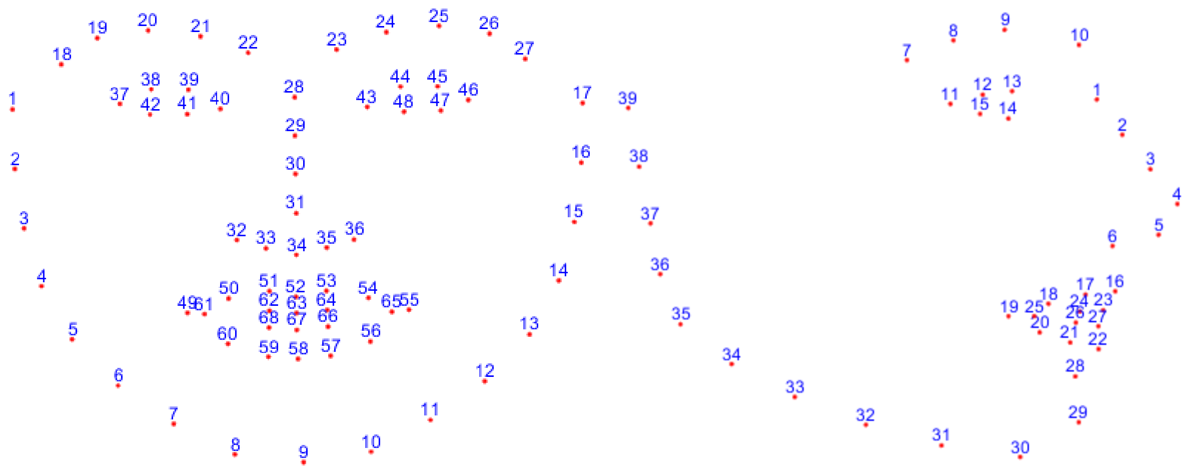

68 point frontal model | 39 point profile model

Figure 4.2: frontal and profile mean shapes

Given a set of training facial images I_i annotated with u fiducial points for each image, the set of all points defines a vector ∈ $\mathcal{R}^{2u*1}$. Figure 4.2 shows the 68 point frontal and 39 point profile mark-up annotations used in this thesis to describe the shape of the human face.

Before any statistical analysis can be performed on the shapes that where obtained from the training set, they need to be aligned to the same coordinate frame. This is done by using Procrustes analysis, which removes the variations in the shapes due to scale, translation and rotation while at the same time retaining all the deformation caused by pose variation, identity and expression. Figure 4.3 illustrates the statistical distribution of facial feature points sampled from 600 facial images, after Procrustes analysis has been applied.

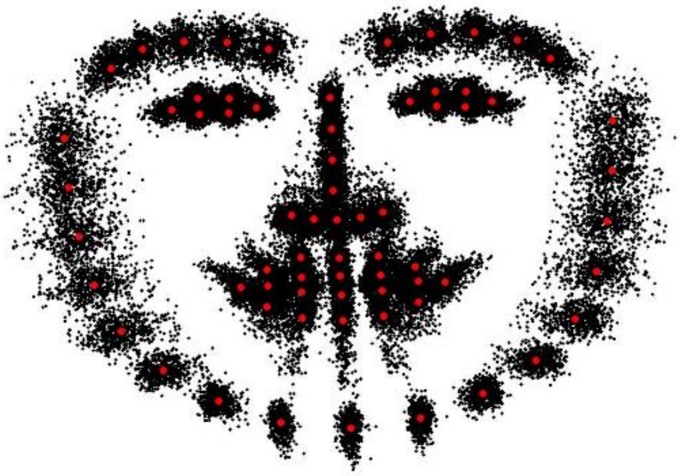

Figure 4.3: Statistical distribution of facial feature points. The black dots represent 600 facial shapes that have been normalised by Procrustes analysis. The red dots signify the mean shape. (Wang et.al, 2014)

Once the shapes in the training set have been normalised, a statistical procedure called Principal Component Analysis (PCA) is applied to obtain the shape model which is defined by a mean shape s_0 and a set of n shape eigenvectors s_i that are represented as columns in $S \in \mathcal{R}^{2u*n}$. These shape eigenvectors capture the variations due to identity, pose and expression.

Finally, in accordance with (Mathews and Barker, 2004) a 2D similarity transform is appended to the shape model, which has four similarity eigenvectors for scale, rotation and translation.

Using this model, a shape can be instantiated by:

$$s(p) = s_0 + Sp \tag{4.1}$$

Where $p \in \mathcal{R}^{n*1}$ is the vector of the shape parameters.

4.1.2 Appearance

To learn the appearance model that is used in PO-CR, similarity transformations are removed from each facial training image I_i this is achieved by warping the image to a reference frame that is defined by the mean shape s_0. As illustrated in Figure 4.4

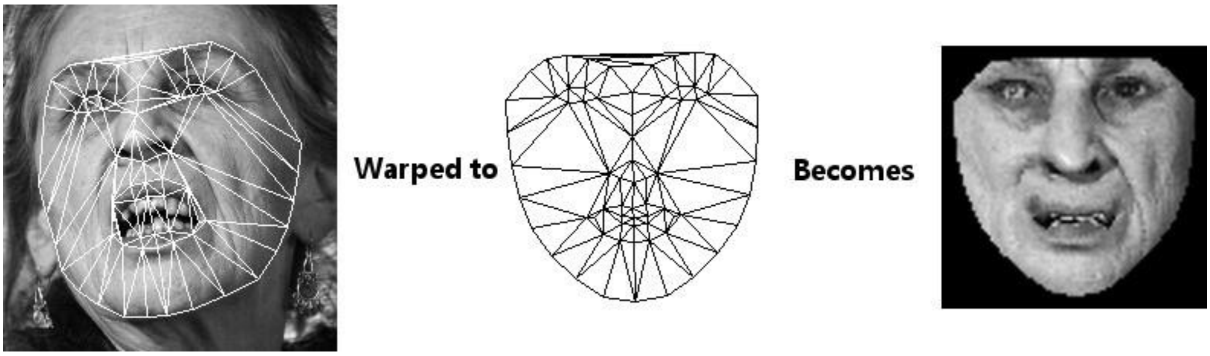

Figure 4.4: Example of a face warped to the mean shape. The left image is the source image taken from a training set with the landmarks triangulated using Delaunay triangulation, the pixels within each triangle are then warped to the corresponding triangle in the mean shape. This gives us the shape-free texture, which is shown in the right image

Next, the local appearance around each landmark is encoded using SIFT (Lowe, 2004) and all the obtained descriptors are stacked in a vector $\in \mathcal{R}^{N*1}$ which defines the part-based facial appearance.

Finally, PCA is applied on all training facial images to obtain the appearance model that is defined by the mean appearance A_0 and m appearance eigenvectors A_i that are represented as columns in $A \in \mathcal{R}^{N*m}$. Using this model, a part-based facial representation can be instantiated by:

$$A(c) = A_0 + Ac \tag{4.2}$$

Where $c \in \mathcal{R}^{m*1}$ is the vector of the appearance parameters.

4.2 Deformable model fitting with PO-CR

We assume that a sub-window of our original image contains a facial image. We also denote by $I(s(p)) \in \mathcal{R}^{N*1}$ the vector obtained by generating u landmarks from a shape instance $s(p)$ and concatenating the computed SIFT descriptors for all landmarks.

To localise the landmarks in the given sub window, the shape and appearance models are fitted by solving the following optimisation problem:

$$\arg\min_{p,c} \|I(s(p)) - A(c)\|^2 \tag{4.3}$$

As Equation (4.3) is non-convex, a locally optimal solution can be readily provided in an iterative fashion using the Lucas Kanade algorithm that was originally proposed by Matthews and Baker, (2004). In particular, given an estimate of p and c at iteration k, linearization of Equation (4.3) is performed and updates, $\Delta p, \Delta c$ can be obtained in closed form. Notably, one can by-pass the calculation of Δc by solving

$$\arg\min_{\Delta p} \|I(s(p)) + J_I \Delta p - A_0\|_P^2 \quad (4.4)$$

where $\|x\|_P^2 = x^T P x$ is the weighted ℓ_2-norm of a vector x. The solution to the above problem is readily given by

$$\Delta p = -H_P^{-1} J_P^T (I(s(p)) - A_0) \quad (4.5)$$

where the projected-out Jacobian matrix is $J_P = PJ_I$ and the projected-out Hessian matrix is $H_P = J_P^T J_P$ and $P = E - AA^T$ is a projection operator that projects out the facial appearance variation from the image specific Jacobian J_I, and E is the identity matrix.

Given that n is the number of shape parameters, m is the number of appearance parameters and N is the number of SIFT features, the above algorithm has a complexity $O(nmN + n^2N)$ per iteration and can be implemented in real-time for a single fitting. But, it is too slow to be employed for all sub-windows of a given image. The reason for this is because the Jacobian matrix, and the inverse Hessian matrix needs to be computed for each iteration.

PO-CR bypasses this computational burden by pre-computing the averaged projected-out Jacobian and Hessian matrices for each iteration using regression.

In particular, for each iteration k PO-CR pre-computes the averaged projected-out Jacobian matrix, denoted as $\hat{J}_p(k)$ as described by (Tzimiropoulos, 2015) which in turn, is then used to pre-calculate the averaged projected-out Hessian matrix, denoted as $\widehat{H}_p(k)$, as follows

$$\widehat{H}_p(k) = \hat{J}_p(k)^T \hat{J}_p(k) \quad (4.6)$$

Finally, the descent directions, denoted as $R(k)$ for each iteration can then be pre-computed by using the inversed average Hessian matrix and average Jacobian matrix

$$R(k) = \widehat{H}_p(k)^{-1}\hat{J}_p(k)^T \tag{4.7}$$

During testing, given a current estimate of the shape parameters at iteration k, denoted as $p(k)$, the image features $I(s(p(k)))$ are extracted and then an update for the shape parameters, $\Delta p(k)$ can be computed as follows

$$\Delta p(k) = R(k)(I(s(p(k))) - A_0) \tag{4.8}$$

Since the descent directions $R(k)$ are pre-computed and A_0 is a constant template representing the mean facial appearance, it is possible to precompute the bias term, denoted as $C(k)$ for each iteration

$$\Delta p(k) = R(k)I(s(p(k))) - R(k)A_0 \tag{4.9}$$

$$C(k) = R(k)A_0 \tag{4.10}$$

which in turn gives the equation

$$\Delta p(k) = R(k)I\left(s\big(p(k)\big)\right) - C(k) \tag{4.11}$$

where $s(p(k))$ is the shape at iteration k, and $R(k) \in \mathcal{R}^{n*N}$ and $C(k) \in \mathcal{R}^{n*1}$ are the descent directions and the bias term for iteration k learned from data using regression. Next, a new estimate for the shape parameters that are used in the next iteration are obtained from

$$p(k+1) = p(k) - \Delta p(k) \tag{4.12}$$

Finally, after L iterations the fitted shape is obtained. Using the above projected-out cascade regression method, the fitting can be achieved with a computational cost of only $O(nN)$. Figure 4.5 demonstrates the high level overview of the proposed Deformable Global Consensus Model.

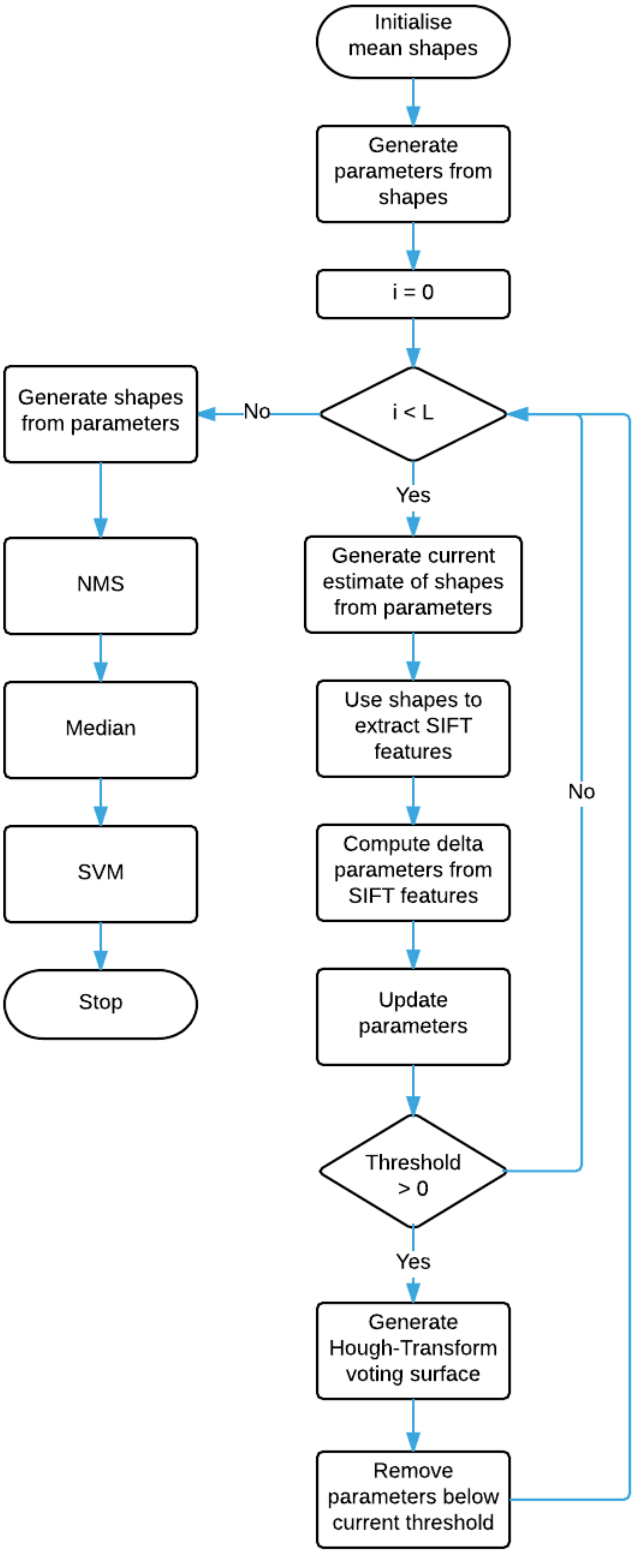

Figure 4.5: Overview of the proposed Deformable Global Consensus Model. For each iteration, if the current threshold is above zero, Hough-Transform voting is used to reject any shapes peaks below the threshold.

4.3 Training

For learning $R(k)$, the training sets of Helen and LFPW plus the available landmark annotations of the 300-W challenge where used to generate the frontal model. This made it possible to fit faces with very large yaw variation $(\pm 70°)$. Because the frontal model could not achieve $\pm 90°$ yaw, another profile model was generated from 1,000 manually annotated profile images from the ALFW dataset.

4.4 Hough-Transform Voting

The proposed DGCM detects faces via a Hough Transform voting scheme by capitalising on the properties of the iterative optimisation procedure employed by PO-CR. The system scans an image in a sliding window fashion using a step of 10 pixels in both the (x, y) dimensions. At each location that is sampled using the sliding window, a facial deformable model is fitted using PO-CR.

Because of the large basin of attraction of regression based approaches, shapes that are initialised close to a face will very likely converge with a high degree of accuracy to that face. On the contrary, shapes that are initialised to the background will converge to random locations. Hence this process will generate a high number of votes for any face within an image, while at the same time will score a low number of votes for background.

Voting in the proposed system is performed in a straight forward fashion. At each iteration the location of the shapes in the image are found by extracting the translational component from p and then for each location a vote is cast. Next, for each iteration, any shapes that belong to a peak that does not pass the threshold value for that iteration are rejected. Finally, because we end up with multiple detections per peak, we apply non-maximum suppression (NMS) (Felzenszwalb, et al., 2010) to reject all low scoring detections that refer to the same face. After which we are left with just a few candidate face locations per image.

For non-maximum suppression (NMS) we adopt a strategy similar to Felzenszwalb, et al., (2010) where we sort scores in descending order, and then iteratively select the detection window with the highest score, while eliminating detected windows with an intersection-over-union (IoU) ratio greater than a predefined threshold to the currently selected detection window.

4.5 Final re-scoring

After the voting phase is finished, we are left with only a few candidate locations. For each of these locations, the median shape is calculated form all the corresponding shapes of each peak, to produce a single fitted shape for that location. Finally, once the final fitted shapes have been obtained, re-scoring of the candidate faces is performed by evaluating an SVM that is trained on both the SIFT features, and the U channel of the LUV colour space as proposed by (Mathias, et al., 2014).

4.6 Complexity

We assume that there are k levels of cascade in the PO-CR model. Then, for each level, a regression matrix $R(k)$ is learned with n regressors and N SIFT features. As stated previously, n is the number of parameters in the shape model. Therefore, the complexity of fitting per sub-window is only $O(K(nN))$.

Because of the large basin of attraction of PO-CR, fitting is performed on a grid of equally spaced points, with a stride of 10 pixels in both the (x, y) dimensions. If there are L locations per image to perform fitting, then the total complexity becomes $O(LK(nN))$ for a single level of the image pyramid.

Furthermore, since the first level of the cascade is optimised for only scale, rotation and translation, and applying a threshold after casting votes in Hough space. The proposed method can reject most of the irrelevant background in the image, which in turn leaves very few locations to be evaluated in the subsequent levels of the cascade. Hence, in practice, the total complexity is $O(LK(nN))$ where K = 1 and n = 4

5 CUDA

In order for the reader to get a good understanding of the fundamentals of parallel programming on the GPU, which is used in this thesis, this chapter introduces the reader to the hardware and software architecture of the CUDA API. We also invite the reader to read Appendix A which gives an in-depth comparison between CUDA and OpenCL, and the reasons why CUDA was chosen over OpenCL.

CUDA stands for Compute Unified Device Architecture and is a parallel programming paradigm, the initial CUDA toolkit 1.0 was release in June 2007 (NVIDIA, 2016).

CUDA is used to develop software that utilises the power of NVIDIA GPU's and cannot be used on GPU's made by any other vendor. As well as graphics, CUDA is also used in many general-purpose, non-graphical applications that are highly parallel in nature. CUDA uses C/C++ as its main programming language, although it also can be programed on other languages like FORTRAN and Java. Since the initial release in 2007, there have been 7 major releases of the CUDA toolkit along with four major hardware revisions; Tesla, Fermi, Kepler and Maxwell.

5.1 CUDA architecture

Figure 5.1: Kepler GK110 Full chip block diagram (Source: NVIDIA, 2012, p6)

The architecture of the GeForce 780ti as illustrated in Figure 5.1 consists of 5 Graphics Processing Clusters (GPC), each containing 3 streaming multiprocessors (SMX), which gives a total of 15 SMX units. Shared 1.5MB L2 cache which can be accessed by all SMX units, six 64-bit memory controllers which gives a combined 384-bit memory interface, that is connected to 3GB of GDDR5 device memory. A Host interface which connects the GPU to the CPU via a PCI-express v3.0 bus and NVIDIA's trademarked GigaThread Engine, which creates and dispatches thread blocks to the various SMX units and manages the context switches between threads during execution.

5.1.1 Streaming multiprocessor (SMX)

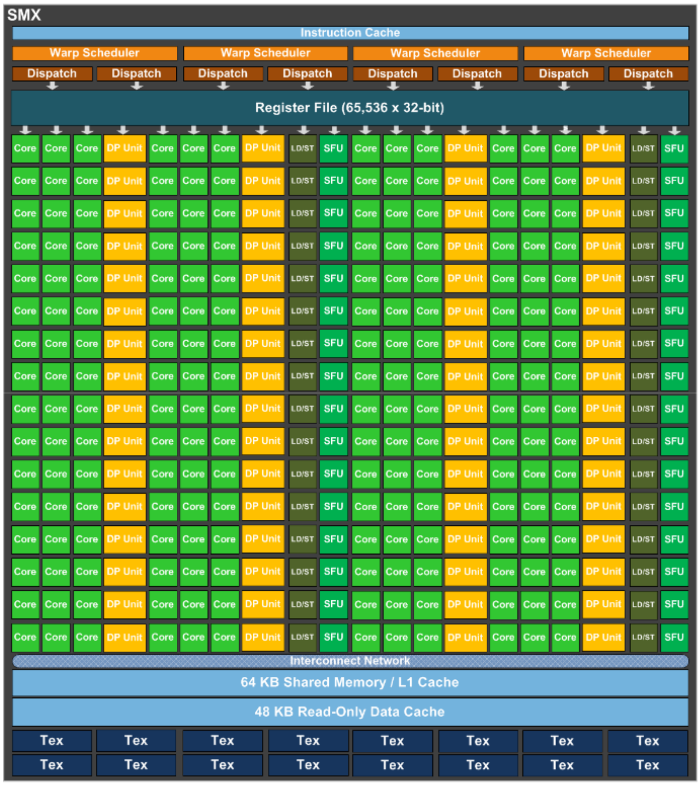

Figure 5.2: SMX: 192 single-precision CUDA cores, 64 double-precision units, 32 special function units (SFU), and 32 load/store units (Source: NVIDIA, 2012, p8)

As shown in Figure 5.2, the SMX unit on the GK110 GPU contains a total of 192 single-precision CUDA cores and 64 double-precision units (DP Unit) which perform arithmetic operations in accordance to the IEEE 754-2008 standard. There are also 32 load/store units (LD/ST) which are used to move data between registers, shared memory and global memory, and 16 special function units (SFU's) which are used for fast approximations of transcendental operations, such as, sin, cosine, reciprocal and square root.

Each SMX also includes 65,536 32-bit registers, an instruction cache, 64 KB of high speed memory that can be partitioned between the L1 cache and shared memory by the developer, and 48 KB of high speed read only data cache memory that is shared by all the CUDA cores on the SMX unit. There are also four warp schedulers and eight instruction dispatch units. The warp schedulers make it possible to issue and execute four concurrent warps, and the instruction dispatch units make it possible to execute two independent instructions of a warp per cycle.

5.2 Compute Capability

NVIDIA use a special term called compute capability to describe different hardware versions of their GPU's. As show in Table 5.1 CUDA comes in several different versions each mapping to a different generation of GPU. Older GPU architectures will not work with a program compiled for higher compute capability devices, however CUDA is backward compatible. With each new revision comes new features and technical specifications.

Architecture	Codename	Compute Capability	Released
Tesla	G80	1.0	2006
	GT200	1.3	2008
Fermi	GF100	2.0	2010
	GF104	2.1	2010
Kepler	GK104	3.0	2012
	GK110	3.5	2013
Maxwell	GM107	5.0	2014
	GM204	5.2	2014
	GM200	5.2	2015

Table 5.1: CUDA Compute Capability

5.3 Kernel Functions

CUDA extends C by allowing the programmer to define C functions which are called kernels, these kernels can only be executed on the GPU, but unlike standard C functions they cannot have a return type. The kernel is defined using the __global__ declaration specifier and the number of threads that execute within the kernel for a given call is specified using the <<<…..>>> execution configuration syntax.

When a kernel function is launched, it creates an array of multiple threads, these threads are mapped to the processor and executed in what NVIDIA call Single-Instruction, Multiple-Thread (SIMT). This is similar to Single-Instruction, Multiple-Data (SIMD), but whereas SIMD requires that all elements in a vector execute together in a unified synchronous group, SIMT allows multiple threads in the same warp to execute independently.

5.4 Thread hierarchy

When a kernel is launched, it is organised into a two-level hierarchy of threads, where the threads are grouped into blocks called thread blocks, and the thread blocks are grouped into a grid, as illustrated in Figure 5.3. There can only be one grid per Kernel. The dimensions of the grid, and thread blocks within the grid, are specified via the execution configuration parameters at kernel launch time by the developer and cannot change throughout the life time of the kernel.

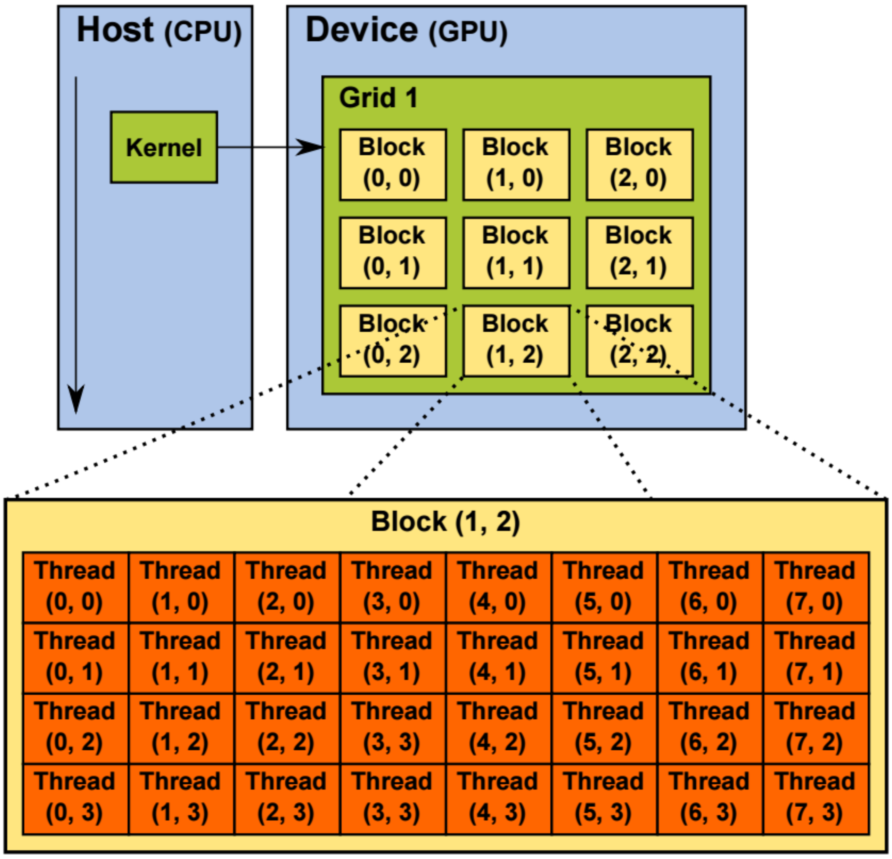

Figure 5.3: Thread hierarchy in the CUDA programming model. (Source: NVIDIA, developer zone, 2015)

As can be seen in Figure 5.3, each thread has a unique local index within its thread block, and every thread block has a unique index within the grid. To help with the indexing of threads within the kernel, CUDA has its own built in variables which are described below:

- **gridDim**: the dimensions of the grid (measured in blocks).
- **blockIdx**: block index within the grid.
- **blockDim**: the dimensions of the block (measured in threads).
- **threadIdx**: thread index within the block.

5.4.1 Thread Blocks

Thread blocks are arranged within the grid in a one, two or three-dimensional formation. An example of a two-dimensional grid can be seen in Figure 5.3. The maximum amount of thread blocks in each dimension that the grid can encompass is limited by hardware.

Thread blocks are required to execute independently from one another, this is because they are distributed randomly to the various SMX units, as and when resources become available. A maximum of sixteen thread blocks can run concurrently in a SMX, but there are several factors that limit this amount, such as the amount of threads, registers and shared memory used per block. Also, it must be noted that because multiple thread blocks execute in parallel, care must be taken to avoid race conditions when writing to global memory, this can be achieved with the use of atomic operators.

5.4.2 Threads

Thread blocks are made up of a collection of threads which run on the CUDA cores. Current hardware supports a maximum of 1024 threads per block which can be arranged in a one, two or three-dimensional formation.

Within a thread block, threads are divided into groups of 32 consecutive threads called warps. The order the warps execute in within the block is random. Threads are only allowed to communicate with other threads in the same block by the use of shared memory. Threads within a warp can also communicate directly with each other using warp level intrinsics. For compute capability 3.0 and above, each thread can have access to a maximum of 255 32-bit registers that are only visible to the thread that they reside in.

The total number of threads that a given kernel executes is equal to the number of threads per block multiplied by the total number of thread blocks. For example, if the execution configuration parameters are set to <<<1024, 256>>> then there will be 1024 thread blocks multiplied by 256 threads, which gives a total of 262,144 threads, executing the same kernel.

5.5 Memory Hierarchy

In the CUDA programming model for the Kepler architecture, the memory hierarchy is composed of four distinct levels, which is illustrated in Figure 5.4. These four levels are from top to bottom (fastest to slowest): the thread level, SMX level, a global level 2 cache and lastly the large global DRAM memory of the GPU.

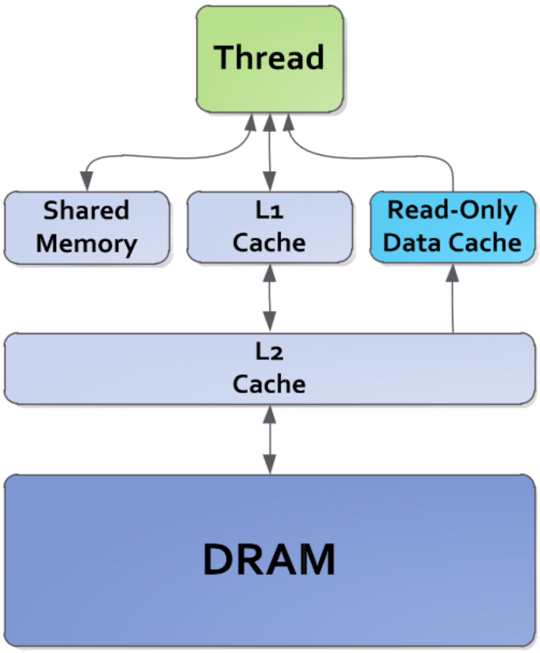

Figure 5.4: Kepler's memory hierarchy (Source: NVIDIA, 2012, p13)

The top level of the memory hierarchy is the thread level. All CUDA cores in an SMX share a total of 65,535 32-bit registers that are partitioned across all resident thread blocks, and each thread has access to a maximum of 255 registers. Depending on the complexity of the kernel, if there are no more resources available then the data is "Spilled" into what is called local memory. In Kepler local memory is stored in the level 1 (L1) cache.

The second level in the memory hierarchy involves shared memory, an L1 cache, and the read-only data cache. Present on each SMX unit is 64KB of very fast on-chip memory which is split into two partitions. The L1 cache which is reserved for local memory accesses such as register spills and stack data, and a user managed partition called shared memory which is visible to all treads within a thread block. Depending on the type of program the L1 cache and shared memory can be configured by the developer to either 16/48KB, 48/16KB or 32/32KB. Shared memory is divided into equally sized memory modules, called banks. If multiple treads from the same warp access different words that map to the same memory bank, we get what is known as a bank conflict. When this happens access to the bank becomes serialised.

In addition to the L1/shared memory cache, a 48KB read only data cache was introduced with devices of compute capability 3.5 and above. This data cache does not have the same bank structure as shared memory and can fully support full-speed unaligned memory access patterns. Use of this cache can be managed automatically by the compiler if it can determine if the data is read only for the life time of the kernel, this is done by qualifying pointers as const and __restrict__, or explicitly by the programmer by using the __ldg() intrinsic function.

The third level in the memory hierarchy contains the global level 2 (L2) cache which has a size of 1.5MB. This cache is the primary point of data unification between all SMX units on the GPU, servicing all load, store, and texture requests to DRAM and providing efficient, high speed data sharing across the GPU. The caching policy which is used is called least recently used (LRU), the main intention of which is to avoid the global memory bandwidth bottleneck (Farber, 2012, p.113).

The bottom level in the memory hierarchy is the DRAM. This is the physical device memory (3GB GDDR5 on the GeForce 780ti) built on the graphics card. Device memory is off-chip and is significantly slower compared to the higher levels in the hierarchy. All threads have access to device memory.

There are also two read-only memory spaces in DRAM which are called constant and texture memory, which can also be accessed by all threads of the GPU. Both constant and texture memory are cached and optimised for different usages. Constant memory is optimised for broadcasting, i.e. when the threads in a warp all read the same memory location, whereas texture memory is optimised for spatial locality.

Constant memory resides in a 64 KB partition of device memory and is accessed through an 8KB cache on each SMX. The texture cache is limited to 48 KB per SMX unit. Both constant and texture memory are persistent across all kernel launches by the same application.

6 Implementation

The proposed system is executed within the MATLAB environment, and Mex-files are used to provide an interface to the CUDA C++ algorithms. Figure 6.1 shows a high level view of the proposed system.

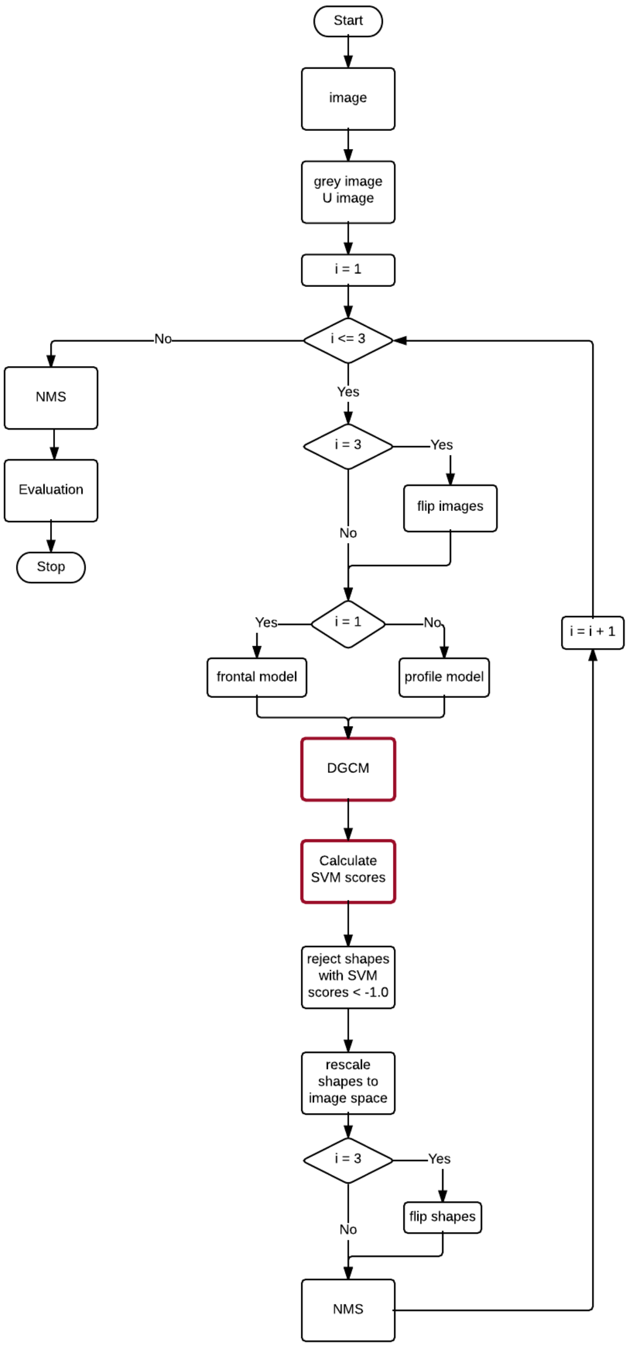

Figure 6.1: System overview, the red outlined boxes are the Mex functions that are used to provide an interface to CUDA C++

Given an RGB image, we first use MATLAB to generate a grey scale image. The RGB image is also converted to LUV colour space using the Mex function "*colorspace*" that was created by Getreuer, (2010), and then the U channel is extracted to be later used in extracting features for the SVM model.

The proposed system needs to iterate three times to cover both frontal and profile (right and left) faces. The three iterations are as follows:

1. Frontal
2. Right profile
3. Left profile

As there are only two models used in the system, a frontal and a right facing profile model, to cover left facing profile faces, the input images (grey scale, U channel) are flipped on the third iteration.

The current model and grey scale image are next passed into the DGCM Mex function, which provides an interface to the CUDA C++ code. DGCM scans the grey scale image over multiple scales, in a sliding window fashion using a step of 10 pixels in both the (x, y) dimensions. For each scale, all sub-windows are simultaneously fitted using the PO-CR algorithm.

After each iteration of the PO-CR algorithm, votes are cast using a Hough-Transform voting scheme for detecting candidate faces and filtering out irrelevant background. For each scale, NMS is applied to remove low level peaks that are within the vicinity of the maxima peaks. Next, the median of the shapes corresponding to each surviving peak is calculated to produce a single fitted shape for each maxima peak. Then the surviving candidate shapes are sent back to MATLAB for further processing.

The remaining candidate shapes are then rescaled back into image space and the left facing profile shapes are flipped back to their original direction. Next, NMS is applied to the remaining candidate shapes to remove low SVM scoring shapes of faces from the wrong scales and then a final NMS is applied on the combined front, left and right shapes. Finally, the performance of the system is evaluated.

6.1 DGCM

The proposed Deformable Global Consensus Model (DGCM) as described in Chapter 4 is implemented in CUDA using two distinct levels of parallelisation. The reason for this is because all the windows of the grid are independent from one another, therefore they can be processed simultaneously, and this is achieved by essentially dedicating one thread block to each instance of the PO-CR fitting algorithm.

6.1.1 Memory allocation

All matrices that are used in the DGCM model are allocated in device memory using the CUDA function call "*cudaMallocPitch*". This guarantees that all the rows of the matrices meet the alignment requirements for coalesced memory accesses. This is achieved by allocating bytes at the end of each row to guarantee that the beginning of the next row starts on a 128 byte memory boundary, as illustrated in Figure 6.2. The pitch is the width of the row including padding measured in bytes.

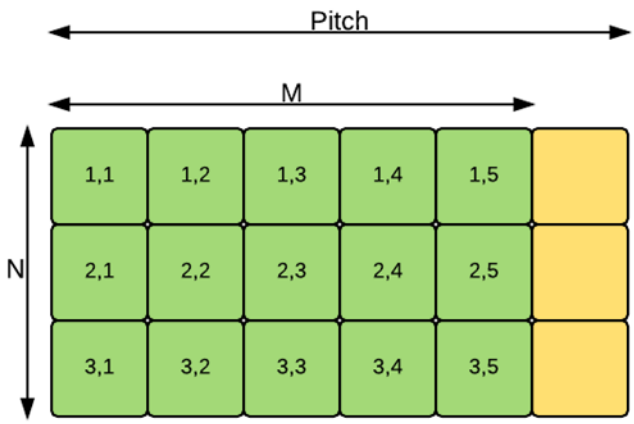

Figure 6.2: 2D matrix allocation. When allocating device memory via the cudaMallocPitch function call, rows are padded (yellow blocks) to guarantee that the beginning of each row begins on a 128 memory boundary.

6.1.2 SIFT

The SIFT descriptor used in this implementation is a variant of Lowes (2004) SIFT keypoint descriptor which is described in Chapter 3.1. Where the main difference is, instead of having a grid containing 16 blocks, that output a 128 element descriptor as shown in Figure 3.1, our variant of Lowes, (2004) descriptor only uses one 8x8 dimensional block, which outputs an 8 element descriptor.

We pre-calculate SIFT descriptors for each pixel in the image and store the results in a texture, which is then used as a look up table. We use texture memory because it is optimised for 2D spatial locality. The pre-calculated SIFT descriptors are stored in a 2D layered texture which has a depth of two. As there are eight descriptor elements per pixel, each layer contains a RGBA texture to hold four descriptors elements.

6.1.3 PO-CR

Given Equation 4.11 and Equation 4.12, the CUDA implementation of the PO-CR fitting algorithm can be broken down into just five stages that consist of four bespoke kernels, which are, for each iteration k:

Stage 1

Calculate the current estimate of the shape parameters $p(k)$. Were $s\big(p(k-1)\big)$ is the shape generated from the previous iteration, S_0 is the mean shape and $Q(k) \in \mathcal{R}^{2u*n}$ contains the combination of the similarity eigenvectors for scale, rotation and translation and the shape eigenvectors

$$p(k) = Q(k)^T * \Big(s\big(p(k-1)\big) - S_0\Big) \tag{6.1}$$

Stage 2

Calculate the current shape $s\big(p(k)\big)$, from the estimate of the shape parameters $p(k)$ that are obtained from Equation (6.1)

$$s\big(p(k)\big) = S_0 + \big(Q(k) * p(k)\big) \tag{6.2}$$

Stage 3

Extract the SIFT features $I\Big(s\big(p(k)\big)\Big) \in \mathcal{R}^{N*1}$ for the current shape, where N is the number of features.

$$I\Big(s\big(p(k)\big)\Big) \tag{6.3}$$

Stage 4

Update the estimate of the shape parameters. Where $R(k)$ and $C(k)$ are the descent directions and bias term as described in Chapter 4.2

$$p(k) = p(k) - \left(\left(R(k) * I\left(s\big(p(k)\big)\right)\right) - C(k)\right) \qquad (6.4)$$

Stage 5

Equation (6.2) is again used to calculate the new shape, using the updated shape parameters $p(k)$ obtained from Equation (6.4)

With the exception of stage 3, in each stage of the PO-CR fitting algorithm the kernel is launched with just one thread block to do all the work in parallel.

The dimensions of the thread block in Equation (6.1) and Equation (6.4) is $(32, n, 1)$ where 32 is the size of a warp and n is the current number of shape parameters $p(k)$. Each row in the thread block calculates the scalar output of the corresponding component of p

In Equation (6.2) the thread block size depends on the amount of points in the shape model, for the 68 point frontal model it is set to $(136,1,1)$ and for the 39 point profile model it is set to $(78,1,1)$.

In Equation (6.3) the thread block size is $(256,1,1)$ and the total number of thread blocks used is calculated by the formula $1 + (((N / 4) - 1) / 256)$ we divide the number of features N by four because we use vectorise access to read four SIFT descriptor elements at a time from texture memory. The value 256 is taken from the thread block's x-dimension.

6.1.4 CUDA Vector-Matrix multiplication

In order to solve Equation (6.1), Equation (6.2) and Equation (6.4), we use vector-matrix multiplication. Given a matrix M and a vector v, it is possible to work out each component of y by calculating the dot product of row i of matrix M with v.

$$y_i = \sum_{j=1}^{n} M_{i,j}\, v_j \qquad (6.5)$$

In parallel computing a dot product can be solved with the use of the reduction primitive. Reduction is one of the most used primitives in parallel computing, it is used to reduce a data sequence into a scaler value using a binary associative operator. It can be used for example to compute the minimum, maximum and sum of two vectors.

Because reduction involves very little processing, it is beneficial to have each thread process multiple elements before doing the actual reduction. This is achieved by each thread reading elements in the arrays in a grid-stride loop (Harris, 2013), and can be further optimised by using vectorised accesses to global memory. Once the loop is completed, then the reduction can be done and the scaler result can be output back to global memory. The code used in this thesis for calculating the dot products is based on a warp shuffle reduction that was explained by Luitjens (2014). Figure 6.3 shows an example of warp shuffle reduction.

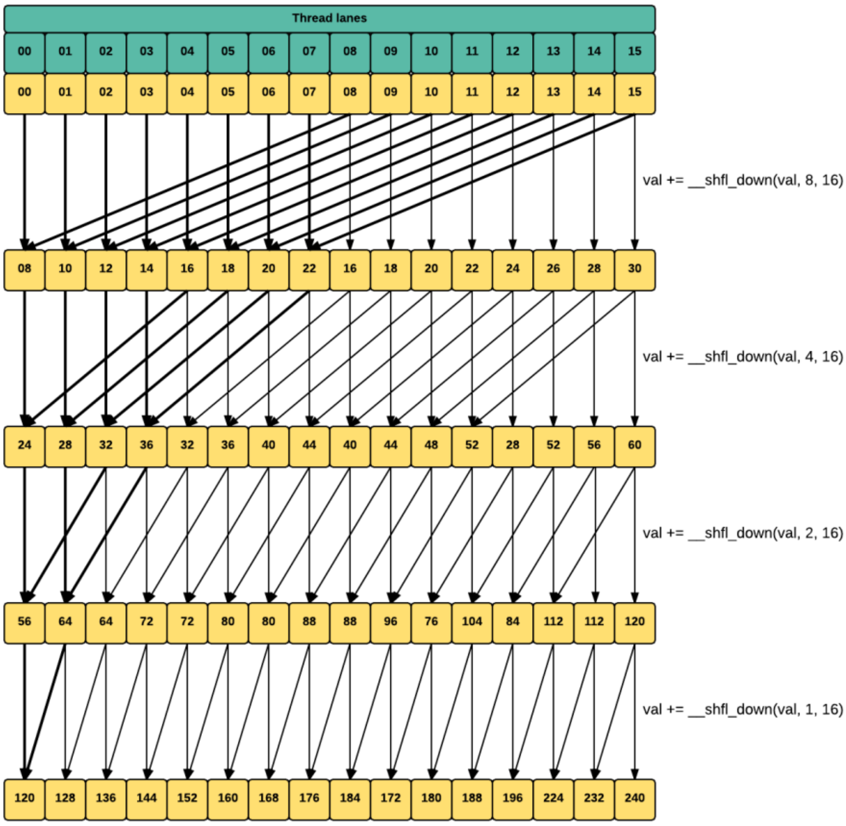

Figure 6.3: Warp reduction using shuffle down, for illustrative purposes this figure only shows a half warp (16 lanes). The first parameter of the __shfl_down intrinsic is the register to return, the second is the offset from the calling lane of the warp and the third parameter is the width of the warp segment which must be of size 2, 4, 8, 16, or 32. The default size is 32.

Figure 6.3 shows how the shuffle down intrinsic is used to build a reduction tree inside a warp. The shuffle down intrinsic first calculates the source lane's ID by adding an offset to the calling lane's ID, and then returns the value held at that location. If the source lane is out of bounds or the source thread has finished, then the value in the calling thread is returned instead. The value that is returned from the source lane is then added to the calling lanes register. Finally, after completing the reduction tree, the thread in lane zero contains the sum of the warp.

6.1.5 Voting

After each iteration of the PO-CR algorithm, the Hough-Transform voting surface is cleared. Next, the location of the shapes in the image are found by extracting the translational component from p and then for each location a vote is cast within an 11*11 grid. Thus, generating peaks on the voting surface, as illustrated in Figure 6.5. Next, any shapes that belong to peaks that do not pass the threshold for the current iteration are rejected, as shown in Figure 6.6 to Figure 6.9. By doing this, it is possible to remove most of the background windows within the first few iterations where the computational cost of calculating $\Delta p(k)$ is relatively cheap. Figure 6.10 shows the SVM scores generated for each peak and Figure 6.11 shows the final fitted shape after a threshold has been applied.

Figure 6.4: Original image from the AFW dataset

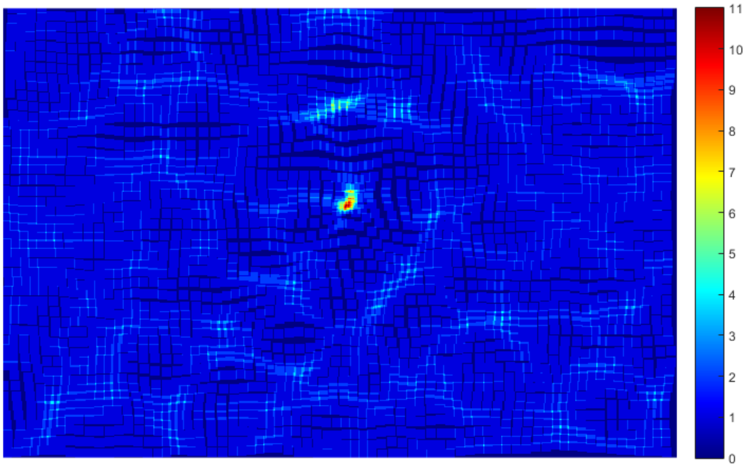

Figure 6.5: Hough-Transform voting surface after first iteration

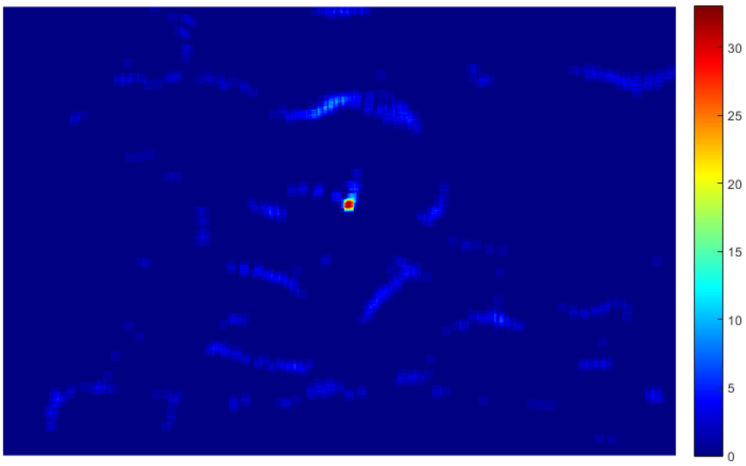

Figure 6.6: Hough-Transform voting surface after second iteration

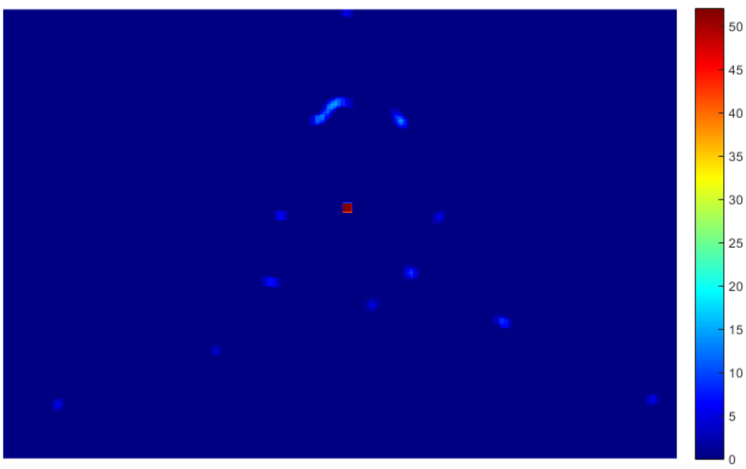

Figure 6.7: Hough-Transform voting surface after fifth iteration

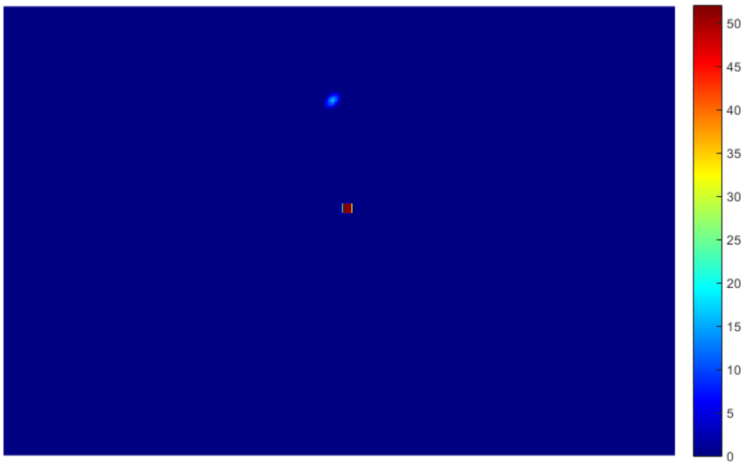

Figure 6.8: Hough-Transform voting surface after tenth iteration

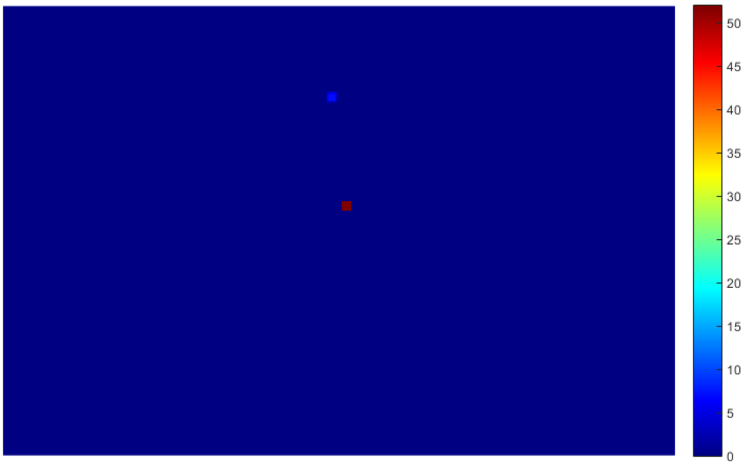

Figure 6.9: Hough-Transform voting surface after fifteenth iteration

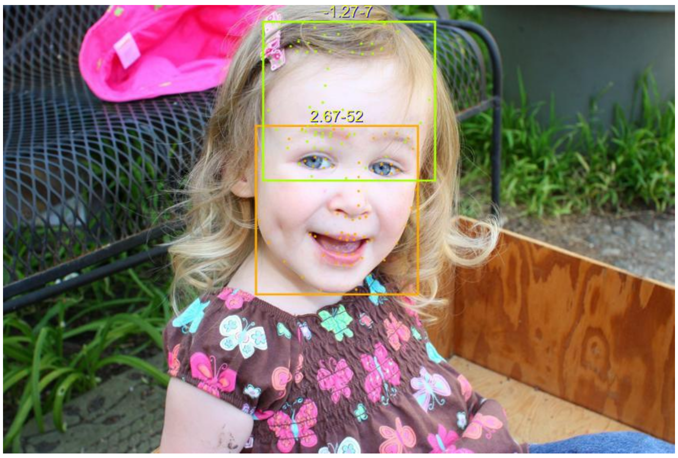

Figure 6.10: SVM scores generated for candidate faces

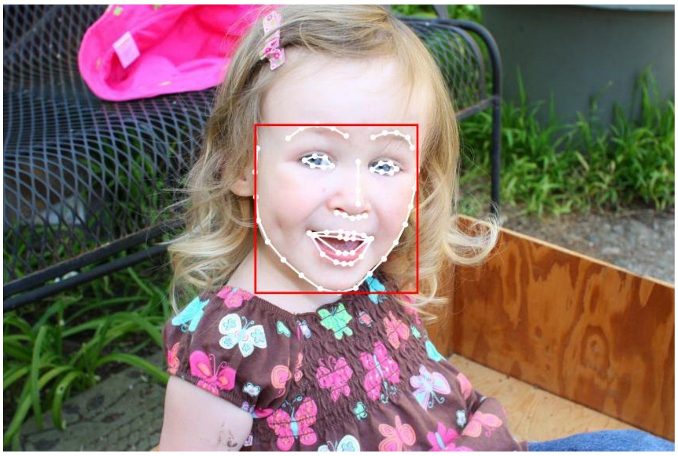

Figure 6.11: Final fitted results after threshold has been applied

In order to remove shapes that have failed the threshold for the current iteration, each shape acquires its vote's score from the Hough-Transform voting surface and stores the result in a votes array. Next, an index array is generated by scanning the votes array and storing the indices of votes that pass the threshold, the indices of votes that fail the threshold are set to minus one, as shown in Figure 6.12.

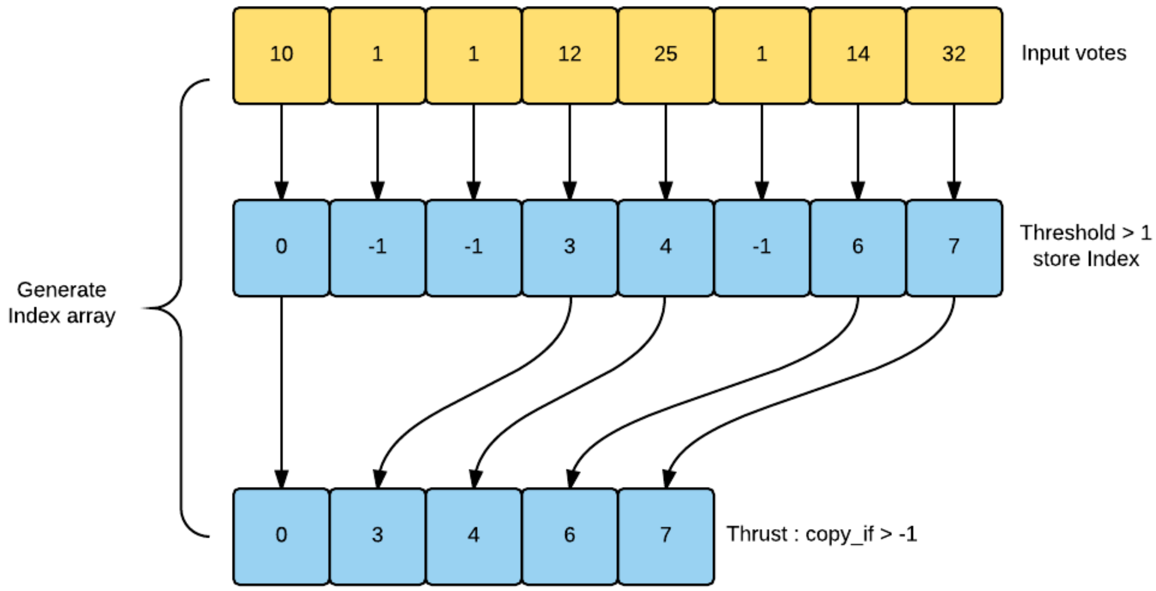

Figure 6.12: Stream compaction. Any vote score (yellow boxes) with a value equal or less than one is set to minus one in the index array, then the function copy_if from the thrust library is used to compact the array.

To compact the index array the function "copy_if" from the Thrust library is used, with the predicate parameter set to minus one. The output of which is a compacted index array. Finally, the new compacted index array is used to get the shapes that pass the threshold.

6.2 Support Vector Machine (SVM)

LIBSVM was used for support vector classification. LIBSVM is an open source library developed at the National Taiwan University. Since version 2.8, it implements a sequential minimal optimisation (SMO) type algorithm which was proposed by (Chang and Lin, 2011).

SVM belongs to the class of maximum margin classifiers and are capable of solving linear and non-linear classification problems. SVMs map data to feature space with the use of kernels. There are four basic kernel functions, linear, polynomial, radial basis function (RBF) and sigmoid.

Given a training set of vectors $x_i \in \mathcal{R}^n, i = 1, \cdots, l$ where each vector belongs to one of two classes that are identified by the label $y_i \in \{-1, 1\}$. The aim of SVM classification is to separate both classes with an optimal separating hyperplane in such a way that the distance to the support vectors is maximised, as illustrated in Figure 6.13, called the maximum margin.

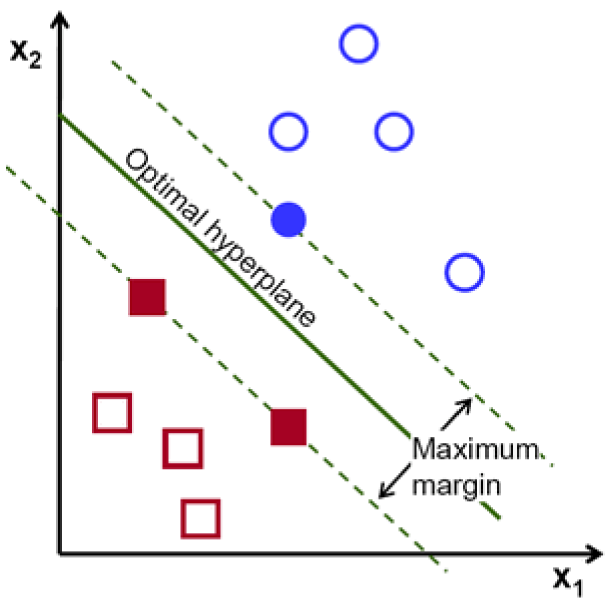

Figure 6.13: Optimal separating hyperplane, the three filled in shapes are the support vectors (Source: OpenCV, 2016)

While optimising an SVM, we are generally looking for two things: a hyperplane with the largest margin, and also a hyperplane that produces the minimum amount of misclassification errors.

The penalty parameter C is a regularisation parameter that controls the cost of misclassification on the training data. Having a low C value generates a large margin separation hyperplane, at the cost of misclassification. While a high C value gives a smaller margin if it does a better job of classifying the training points correctly. Finding the optimal C value while minimising overfitting is generally done with the use of cross-validation.

6.2.1 Feature normalisation

Before using cross validation to find the optimal value of C, both the SIFT and colour features (LUV colour space, U channel) (Mathias et al, 2014) needs to be normalised. We found that the best method to normalise these features was to use zero-mean ℓ_2-norm. This is achieved by first, calculating the zero-mean

$$\mu = {}^{1}/_{N} \sum_{i=1}^{N} x_i \tag{6.6}$$

$$x_i = x_i - \mu \tag{6.7}$$

Next, the features are normalised, and weight adjusted, for SIFT Vectors the value of w is set to 1 and for the colour vectors 0.2 is used

$$x_i = (x_i/|x|) * w \tag{6.8}$$

Finally, the normalised SIFT and colour features are combined into a single vector.

6.2.2 Cross-validation

LIBSVM has an option –v to set the number of folds to use in cross-validation. For example, using –v 5 creates 5-folds, where the training data is split into 5 equally sized subsets, and each subset is then tested using a classifier trained on the remaining 4 subsets.

In order to find the optimal C value and prevent overfitting, a grid-search on C is performed using cross-validation. This is done by first scanning a coarse 1-dimensional grid to find the highest cross validation accuracy region. Then, a finer scan is conducted in that region to find the optimal C value. Once the optimal C parameter has been found the model can be trained using all the training data.

6.2.3 Training

For training the SVM model, a two-step approach was used. First, DGCM scans the training sets and then all the fitted shapes are stored in the positive class. The negative class is obtained by sorting the votes of the background shapes in descending order, next they are truncated it to match the size of the positive class, then a SV is trained.

Next, DGCM is again used to scan the training sets, but this time it also calculates the SVM scores for the shapes. As before, the shapes are split into positive and negative classes, but this time the negative class is sorted in descending order using the SVM scores. Finally, the negative class is truncated to match the size of the positive class, before generating the final SVM model.

6.2.4 Classification

Once the optimal separating hyperplane has been found, the SVM can attempt to classify unseen data. Given an instance z it can be classified by determining which side of the decision boundary it belongs to, by computing the following decision function

$$f(z) = sign\left(\sum_{i=1}^{totalSV} y_i \alpha_i k(x_i, z) + \rho\right) = sign(w^T \phi(z) + \rho) \qquad (6.9)$$

where y is the training labels, α contains the support values, $k(.,.)$ is the kernel function, ρ is the offset from the origin and w defines the normal to the hyperplane.

Within the LIBSVM model that is generated in the training phase, sv_coef contains $\alpha_i y_i$, SVs contains the support vectors x_i, and $-rho$ is the ρ value

Using a linear kernel $k(x, z) = x^T z$ it is possible to compute w explicitly using

$$w = SVs^T * sv\_coef \qquad (6.10)$$

Therefore, all predictions are simply based on the function.

$$z^T w + \rho \tag{6.11}$$

If the score is larger than the defined threshold we then classify the candidate window as a face.

7 Results

In order to evaluate the performance of our proposed system, all tests were done using a NVIDIA GeForce GTX 980 GPU and an Intel I7-4790k CPU, on a PC running Windows 8.1 64-bit with 16GB of ram. The proposed system was compiled for GPU devices of compute capability 3.5 and above, using CUDA 7.0 development toolkit.

7.1 Performance measures

For face detection, faces are only considered detected if the intersection-over-union (IoU) ratio between the ground truth and the detected bounding box/ellipse exceeds 0.5 (50%) (Everingham et al, 2009). Given a detected bounding box B_d and ground truth bounding box B_{gt} the area of overlap a_o can be found using the formula

$$a_o = \frac{area(B_d \cap B_{gt})}{area(B_d \cup B_{gt})}$$

where the intersection $B_d \cap B_{gt}$ is the area of overlap between the detected and ground truth bounding boxes and the union $B_d \cup B_{gt}$ is the sum of the areas of both bounding boxes minus the intersection.

To evaluate the performance of our experiments for face detection on the AFW dataset, we use a precision-recall (PR) curve to extract the relationship between the detection rate (recall) and detection accuracy (precision).

Precision and Recall are defined as:

$$precision = \frac{TP}{TP + FP}$$

$$recall = \frac{TP}{TP + FN}$$

Where true positives TP are faces that are correctly classified. False positives FP is where the detector wrongly classifies background as a face, and false negatives FN are faces that are not detected.

For the facial landmark experiments, the proposed system DGCM is compared against the combined state-of-the-art pipeline of Head-Hunter (Mathias et al. 2014) and PO-CR (Tzimiropoulos, 2015). To measure the performance of landmark localisation, tests where done using the point-to-point Euclidean distance (pt-pt error) which is normalised by face size and report the cumulative curve corresponding to the fraction of images for which the error was less than a specific value as proposed by (Zhu and Ramanan, 2012).

7.2 Face detection

To evaluate the performance of face detection, two of the most popular "in the wild" datasets where used.

- AFW (Zhu and Ramanan, 2012) the annotated faces in-the-wild (AFW) dataset is built from images from Flickr. It consists of 205 images with a total of 474 annotated faces (Mathias et al. 2014), the images within this dataset tend to contain cluttered background and faces with large variations in both viewpoint and appearance
- FDDB (Jain and Learned-Miller, 2010) the Face Detection Dataset and Benchmark (FDDB) dataset consists of 2,845 images, with a total of 5,171 ellipse face annotations. This dataset includes very challenging low resolution, out of focus and occluded faces.

7.2.1 Annotated faces in-the-wild

On the AFW dataset we compare the performance of our proposed detector against current published and commercial state-of-the-art methods including: Head-Hunter (Mathias et al. 2014), DPM (Mathias et al. 2014), SquaresChnFtrs-5 (Mathias et al. 2014), Tree Parts Model (TSM) (Zhu and Ramanan, 2012), Structural Models (Yan et al, 2013), Shen et al (2013) and commercial systems Face.com and Face++.

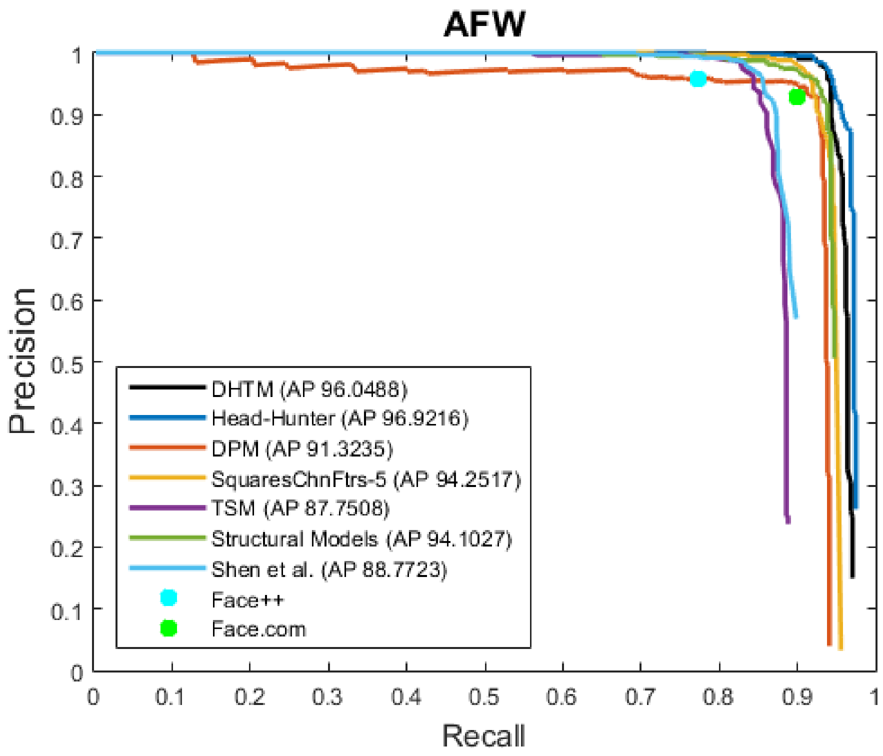

Figure 7.1: Precision-Recall curve of different evaluation methods on the AFW dataset. With Intersection-over-Union (IoU) overlap set to 50%

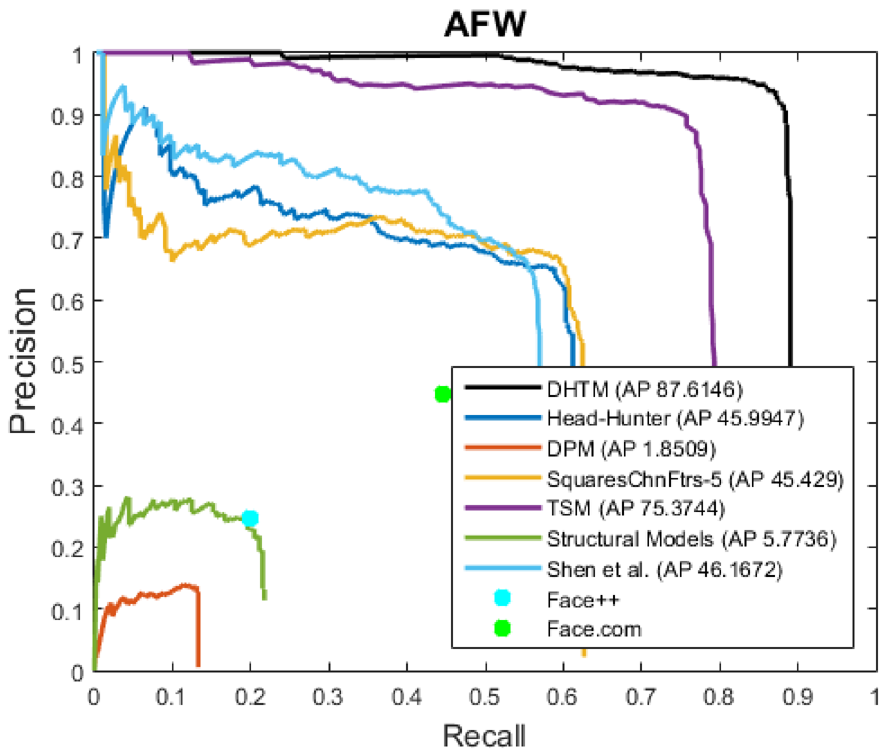

Figure 7.2: Precision-Recall curve of different evaluation methods on the AFW dataset. With Intersection-over-Union (IoU) overlap set to 75%

As illustrated in Figure 7.1, on the AFW dataset with the IoU overlap set to 50%, we show that our detector is comparable to both current commercial and published state-of-the-art methods. To further show the accuracy of our proposed detector, we increased the IoU overlap to 75%, and as can be seen in Figure 7.2, our detector clearly outperforms all commercial and published methods by a margin of over 10% in detection accuracy.

7.2.2 Face Detection Dataset and Benchmark

FDDB defines two types of evaluations: the discrete score and continuous score. For evaluating the discrete score, it counts the number of true positives (detected faces) against the number of false positives. Detected faces are only considered as true positive if the IoU ratio to the ground truth ellipse exceeds 0.5. In the continuous score evaluation, it evaluates the accuracy of the detected bounding ellipse against the ground truth ellipse, by using the IoU ratio as the matching metric.

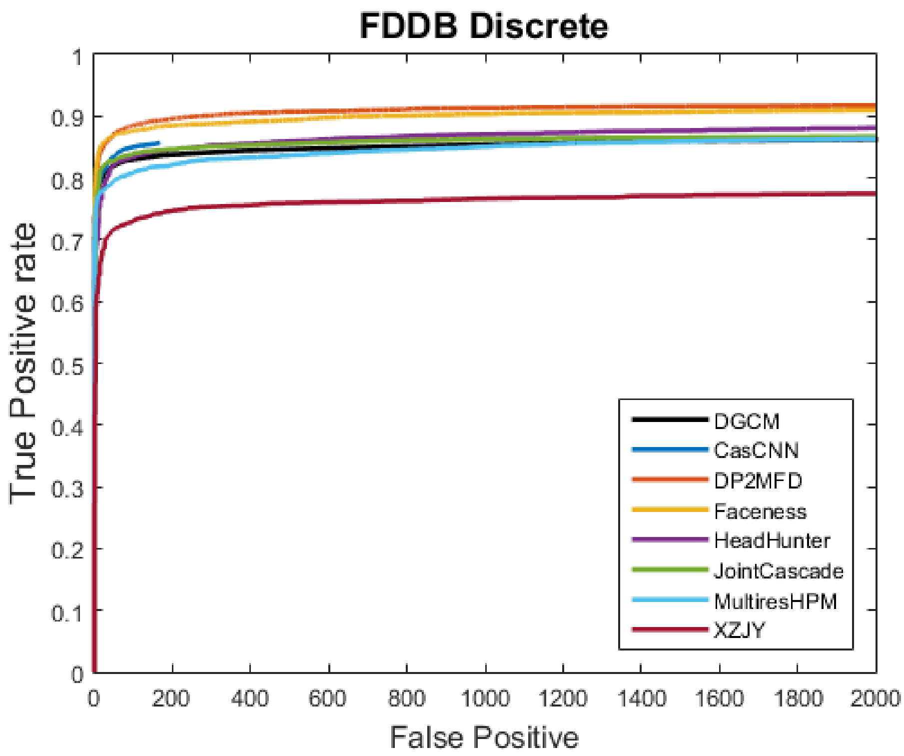

Figure 7.3: FDDB Discrete scores.

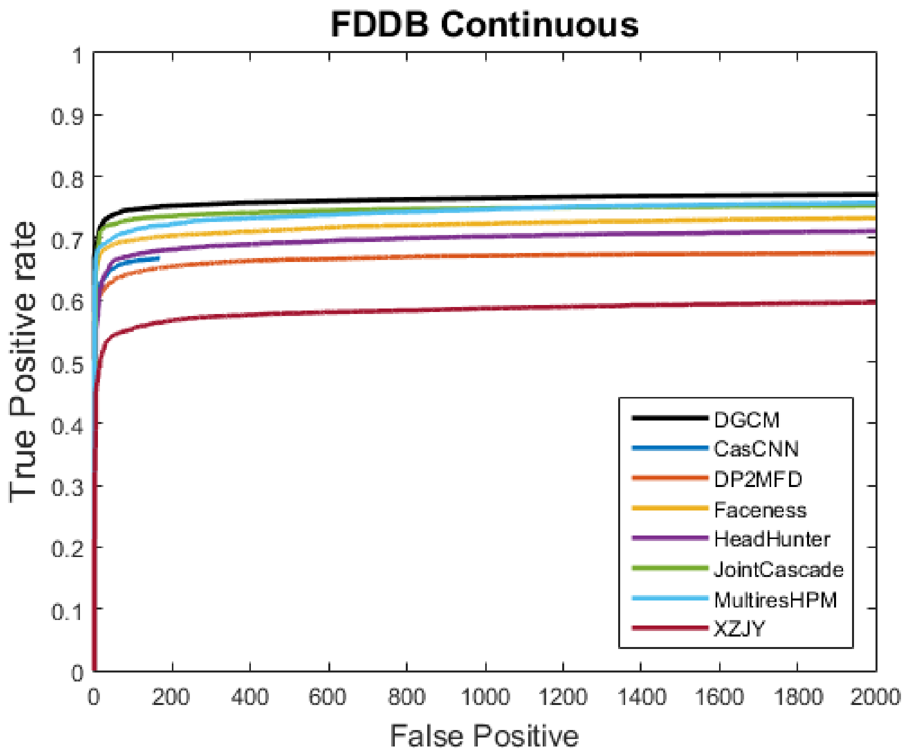

Figure 7.4: FDDB Continuous scores (true positive ratio is IoU between detection ellipse and ground-truth ellipse.)

On the FDDB dataset we compare the performance of our proposed detector against the current published state-of-the-art methods including: CasCNN (Li et al, 2015), DP2MFD (Ranjan, Patel and Chellappa, 2015), Faceness (Yang et al, 2015), HeadHunter (Mathias et al. 2014), JointCascade (Chen et al, 2014), MultiresHPM (Ghiasi and Fowlkes, 2015) and XZJY (Shen et al, 2013).

For discrete scores, as show in Figure 7.3, the performance of our system seems to be on par with that of published state-of-the-art methods. For continuous scores, Figure 7.4, we show that our detector outperforms all published state-of-the-art methods for accuracy.

7.3 Landmark localisation

To evaluate the performance of landmark localisation a large number of experiments where conducted on the most challenging facial databases.

- AFW (Zhu and Ramanan, 2012) as described in 7.2.
- COFW (Burgos-Artizzu, Perona and Dollár, 2013) the Caltech Occluded Faces in the Wild (COFW) dataset contains 507 annotated faces that are set in real

world conditions. The faces tend to have large variations due to pose and expression, and over 23% of faces have various degrees of occlusion.

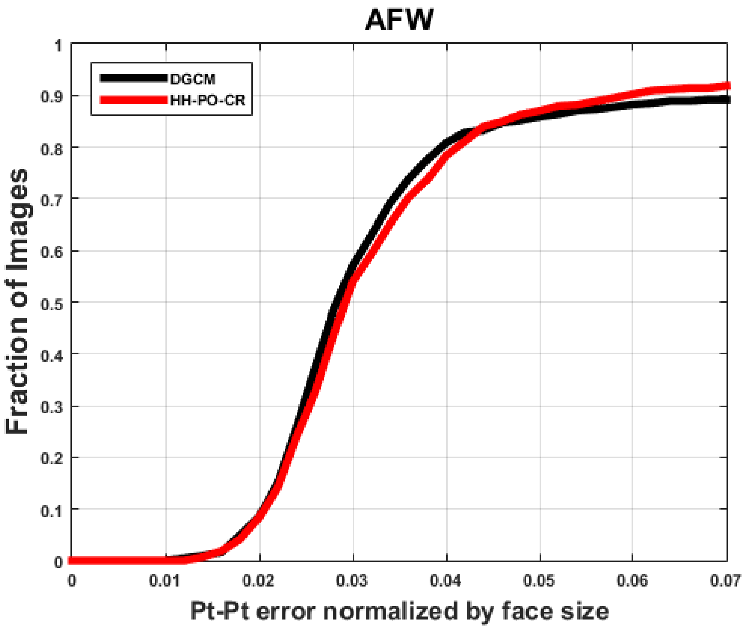

Figure 7.5: Accumulated point-to-point error, relative to size of face, for 474 annotated faces from the AFW dataset.

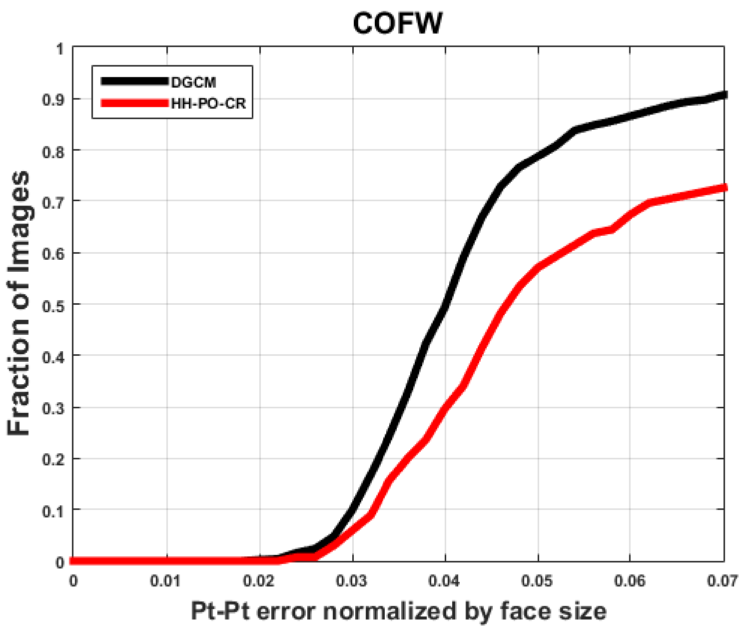

Figure 7.6: Accumulated point-to-point error, relative to size of face, for 507 annotated faces from the COFW dataset.

For landmark localisation, as can be seen in Figure 7.5, the proposed system of this thesis, DGCM, shows comparable performance to that of the state-of-the-art pipeline of Head-Hunter (Mathias et al. 2014) and PO-CR (Tzimiropoulos, 2015) on the AFW dataset. Also, Figure 7.6 clearly shows that DGCM outperforms the combined pipeline of Head-Hunter and PO-CR by approximately 20% on the COFW dataset. This is because of the inaccuracies of head-hunter's face detector, which makes it a lot harder for the PO-CR fitting algorithm to fit to occluded faces.

7.4 Execution times

All experiments were done on a 640*480 VGA image from the AFW dataset (2844520516.jpg). The image pyramid was calculated using the formula $ceil\left((1/1.1^{scale}) * imageSize\right)$ and a step size of 10 pixels was used.

Scale factor	Grid size	Initial number of windows	Frontal Time ms	Right Profile Time ms	Left Profile Time ms
2.14	138 x 103	14214	96.092201	81.077698	71.068100
1.95	125 x 94	11750	79.075699	68.065300	60.057598
1.77	114 x 86	9804	72.069099	59.056801	57.054901
1.61	104 x 78	8112	64.061401	48.046101	50.048000
1.46	94 x 71	6674	55.053101	41.039101	43.041000
1.33	86 x 64	5504	45.043098	34.032600	37.035702
1.21	78 x 59	4602	39.037201	32.030701	37.035801
1.10	71 x 53	3763	36.034599	32.030701	34.032398
1.00	64 x 48	3072	32.030899	27.025900	29.028099
0.91	59 x 44	2596	31.029499	27.025900	27.025299
0.83	53 x 40	2120	26.025200	23.022100	22.021400
0.75	49 x 37	1813	27.025700	24.023001	20.019199
0.68	44 x 33	1452	24.023199	20.019400	17.016300
0.62	40 x 30	1200	21.019899	17.016100	15.014400
0.56	37 x 28	1036	19.018299	16.015400	14.013200
0.51	33 x 25	825	16.015301	13.012700	13.012500
0.47	30 x 23	690	10.009600	14.013200	13.012400
0.42	28 x 21	588	13.012500	13.012700	8.008000
0.39	25 x 19	475	14.013400	14.013200	8.007400
0.35	23 x 17	391	13.012200	13.012700	8.007700
		Total execution time in ms	**732.702095**	**616.591304**	**583.559397**

Table 7.1: Scaling factors and resulting grid dimensions of a VGA image, with execution times for frontal, right profile and left profile models measured in milliseconds

Table 7.1 shows the execution times to scan for faces (frontal and profile) of size 80*80 to image size in a VGA image. For each layer in the image pyramid we include the timings for image resizing, generating SIFT images, scanning and returning the results to MATLAB. All execution times are measured in milliseconds. We show the individual timings for each layer of the pyramid and the total times for frontal plus left and right profile faces.

7.5 Images

Below are some examples of images with extreme pose, expression and occlusion from the AFW, FDDB and COFW datasets, which show how accurate the proposed system is at unified facial detection and landmark localisation.

7.5.1 AFW

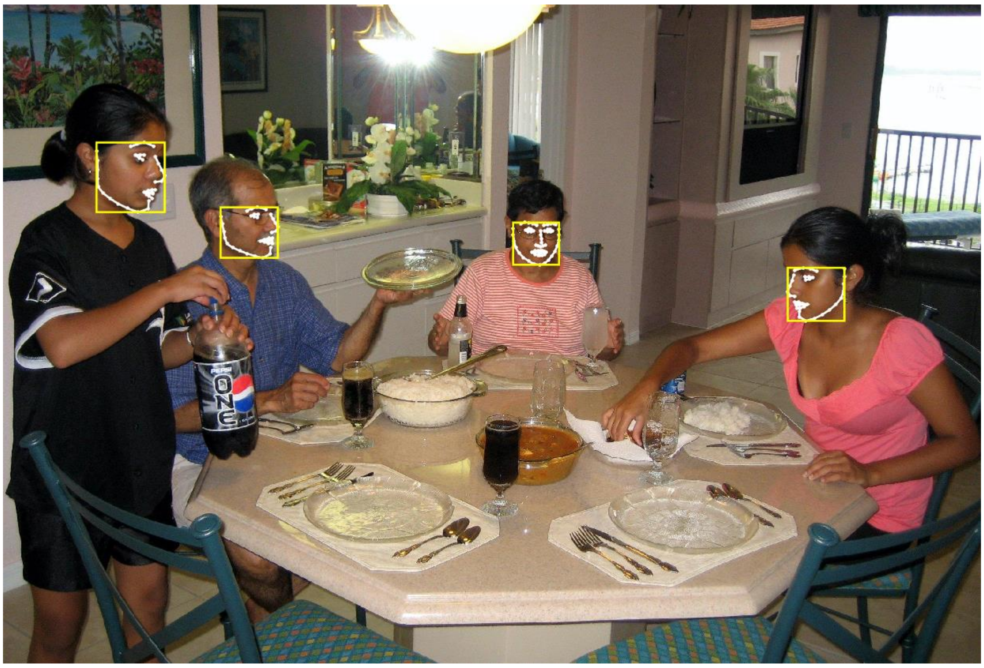


OHIO STATE
M-F ATHLETIC
OHIO STATE
UNIVERSITY

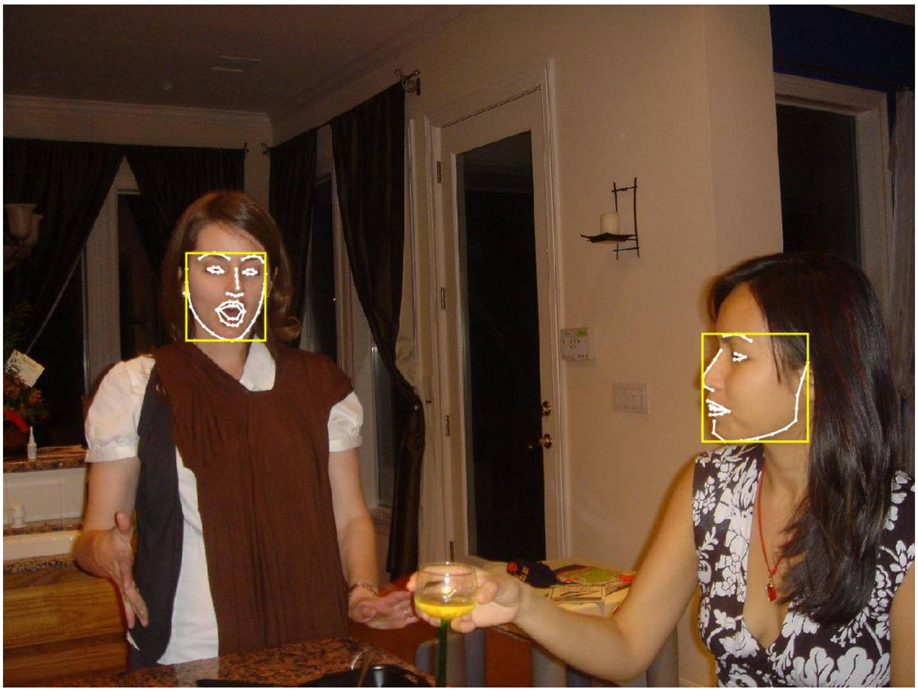

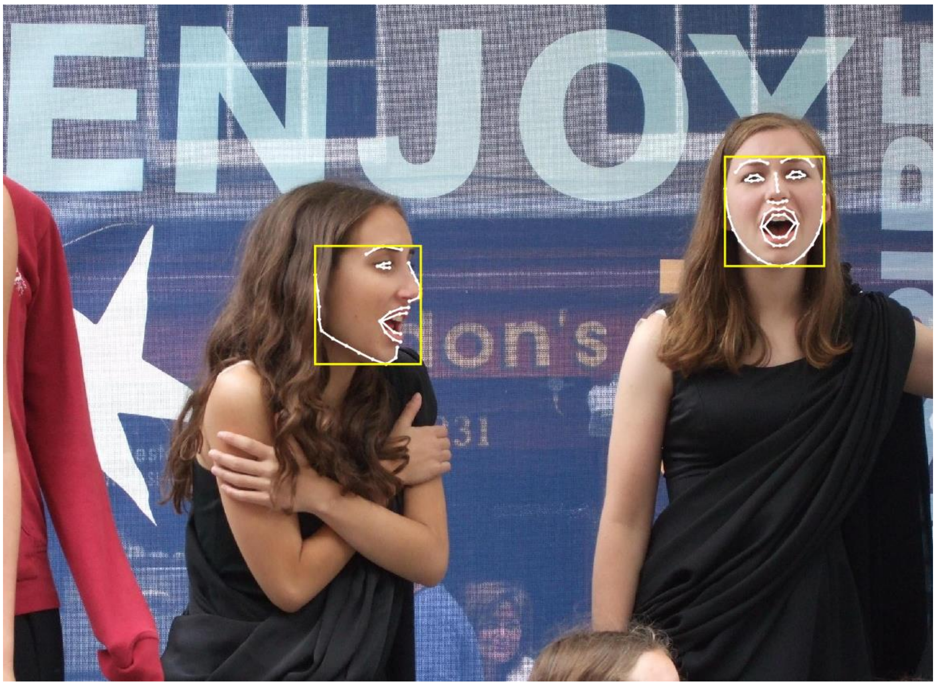

7.5.2 FDDB

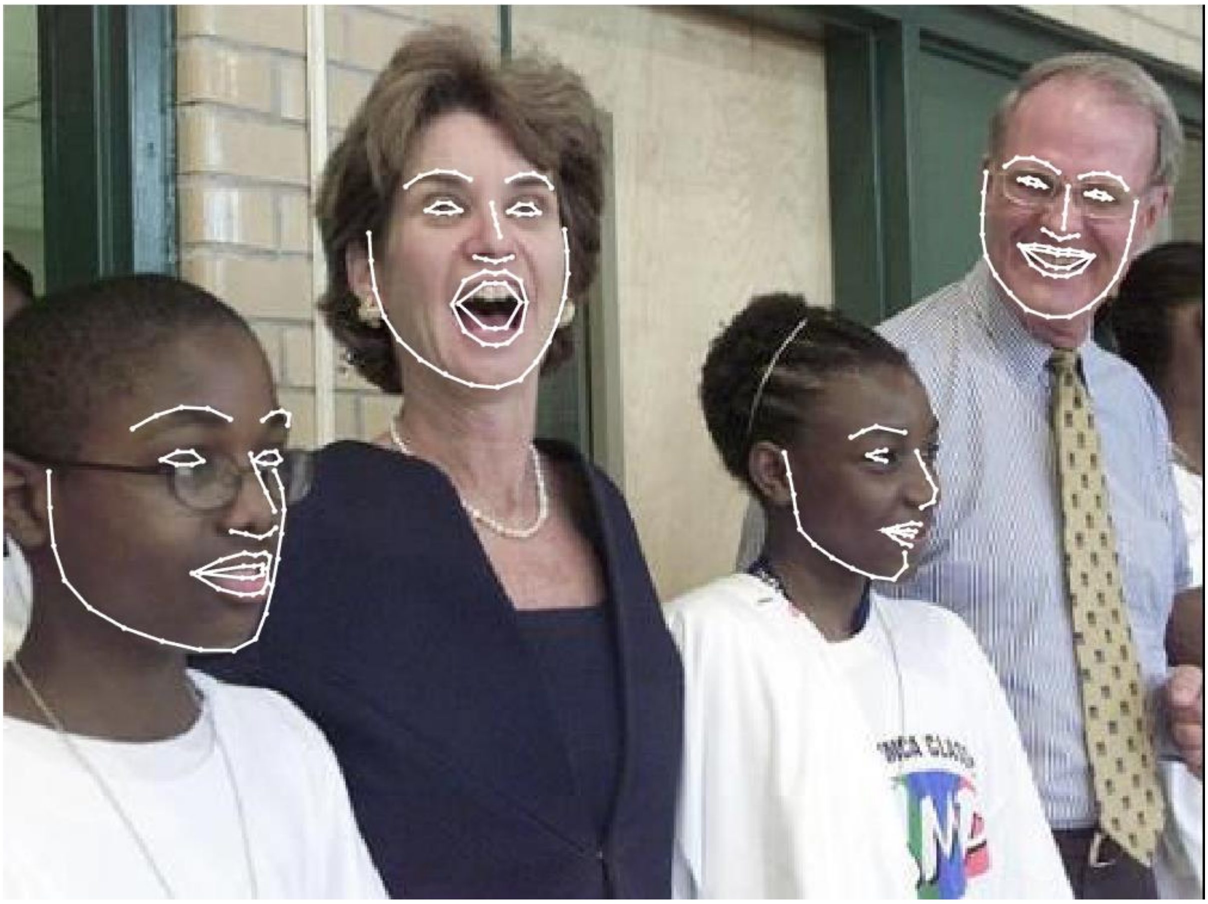


オーベントー

7.5.3 COFW


特惠机票





8 Conclusion

This thesis proposes a novel approach to face detection and landmark localisation which is termed the Deformable Global Consensus Model (DGCM). DGCM is largely motivated by the efficiency and robustness of recent Cascaded Regression (CR) methodologies in facial alignment. But, whereas standard approaches use a face detector to initialise them, the proposed system of this thesis instead, utilises them in a parallel fashion, order to detect the location of faces in an arbitrary image.

We report comparable performance to that of published state-of-the-art face detection algorithms, but as can be seen in Figure 7.2, Figure 7.4 and Figure 7.6 we also show that the proposed system also detects faces with a higher degree of accuracy. We also report significant improvement over the standard face detection/landmark localisation pipeline when performance is measured in terms of landmark localisation.

We also demonstrate that real-time scanning of an arbitrary VGA image can be achieved as long as the face size is known in advance, Table 7.1.

Figure 8.1: FDDB dataset. Example of low resolution missed faces. Yellow ellipses show faces that are detected, and red ellipses show faces that are not detected

Even though the proposed system is more accurate than current state-of-the-art systems, it is still not without its problems. One of the main problems was that PO-CR was trained with just two high resolution models, one model for frontal and another for profile faces. As can be seen in Figure 8.1, this lead to a lot of missed detections in the FDDB dataset. Having a second low resolution model trained for both frontal and profile faces should rectify this problem.

9 Reference

Al-Shehri, S. A., 2004. A Simple and Novel Method for Skin Detection and Face Locating and Tracking [pdf] Springer. Available at: http://link.springer.com/chapter/10.1007%2F978-3-540-27795-8_1 [Accessed on 17 January 2016].

AnandTech, 2015. *NVIDIA Posts 350.05 Hotfix Driver – Fixes Games & adds OpenCL 1.2 Support.* [online] Available at: http://www.anandtech.com/show/9139/nvidia-posts-35005-hotfix-driver-fixes-games-adds-opencl-12-support [Accessed 25 June 2015].

Asthana, A., Saragih, J., Wagner, M. and Goecke, R., 2009. *Evaluating AAM fitting methods for facial expression recognition*. ACII, pp.1–8.

Belhumeur, P., Jacobs, D., Kriegman, D, and Kumar, N., 2011. *Localizing parts of faces using a consensus of exemplars*. CVPR, pp.545-552.

Bernabé, G., Guerrero, G. and Fernández, J., 2012. *CUDA and OpenCL Implementations of 3D Fast Wavelet Transform*. [pdf] Available at: http://ditec.um.es/caps/pdfs/bernabe_lascas12.pdf [Accessed 26 June 2015].

Brown, M. and Lowe, D.G., 2002. *Invariant Features from Interest Point Groups*. [pdf] British Machine Vision Conference. Available at: http://www.comp.leeds.ac.uk/bmvc2008/proceedings/2002/papers/92/full_92.pdf [Accessed 19 June 2015].

Burgos-Artizzu, X.P., Perona, P. and Dollár, P., 2013. *Robust face landmark estimation under occlusion*. ICCV, pp.1513-1520.

Cao, X., Wei, Y., Wen, F. and Sun. J., 2012. *Face alignment by explicit shape regression*. IJCV, 107(2), p.177-190

Chang, C.-C. and Lin, C.-J., 2011*. LIBSVM: a library for support vector machines.* ACM Transactions on Intelligent Systems and Technology. 2(3) p.27:1==27:27

Chen, D., Cao, X., Wen, F. and Sun, J., 2013. *Blessing of dimensionality: High-dimensional feature and its efficient compression for face verification*. CVPR, pp.3025–3032.

Chen, D., Ren, S., Wei, Y., Cao, X., and Sun. J., 2014. *Joint cascade face detection and alignment*. ECCV, 8694, pp.109-122.

Chew, S.W., Lucey, P., Lucey, S., Saragih, J., Cohn, J.F., Matthews, I. and Sridharan, S., 2012. *In the pursuit of effective affective computing: The relationship between features and registration*. IEEE SMC-B, 42(4), pp.1006-1016.

Cootes, T. F., Edwards, G. J. and Taylor, C. J., 1998. *Active appearance models*. Proceedings of the European Conference on Computer Vision, vol. 2, pp.484–498.

Cootes, T., Edwards, E., and Taylor, C., 2001. *Active appearance models*. TPAMI, 23(6), pp.681–685.

Cootes, T. F., Edwards, G. J. and Taylor, C. J., 2001. *Active appearance models*. Pattern Analysis and Machine Intelligence, IEEE Transactions 23(6), pp.681-685.

Cootes, T. F. and Taylor, C. J., 1992. *Active shape models — 'Smart Snakes'*. BMVC92, pp.266-275.

Cristinacce, D. and Cootes, T., 2006. *Feature detection and tracking with constrained local models*. [pdf] University of Manchester. Available at: http://personalpages.manchester.ac.uk/staff/timothy.f.cootes/papers/BMVC06/cristinacce_bmvc06.pdf [Accessed on 2 October 2015].

DolÍar, P., Welinder, P. and Perona, P., 2010. *Cascaded pose regression*. [pdf] Available at: http://vision.ucsd.edu/~pdollar/files/papers/DollarCVPR10pose.pdf [Accessed on 2 December 2015].

Everingham, M., Van Gool, L., Williams, C.K.I., Winn, J. and Zisserman, A., 2009. *The PASCAL Visual Object Classes (VOC) Challenge*. [pdf] Available at: http://homepages.inf.ed.ac.uk/ckiw/postscript/ijcv_voc09.pdf [Accessed on 20 January 2016].

Fang, J., Varbanescu, A. L. and Sips, H., 2011. *A Comprehensive Performance Comparison of CUDA and OpenCL.* Parallel Processing (ICPP), International Conference. IEEE, pp.216-225

Farber, R., 2012. *CUDA application design and development*. Waltham:Morgan Kaufmann.

Felzenszwalb, P.F., Girshick, R.B., McAllester, D. and Ramanan, D., 2010. *Object Detection with Discriminatively Trained Part Based Models* [pdf] Available at: https://www.cs.berkeley.edu/~rbg/papers/Object-Detection-with-Discriminatively-Trained-Part-Based-Models--Felzenszwalb-Girshick-McAllester-Ramanan.pdf [Accessed on 12 December 2015].

Getreuer, P., 2010. Colorspace Transformations [online] MATLAB Central. Available at: http://uk.mathworks.com/matlabcentral/fileexchange/28790-colorspace-transformations [Accessed on 1 November 2015].

Ghiasi, G. and Fowlkes, C.C., 2014. *Occlusion coherence: Detecting and localizing occluded faces.* [online] Cornell University Library. Available at: http://arxiv.org/abs/1506.08347 [Accessed 30 November 2015].

Gil, L., 2013. *A Short introduction to descriptors* [blog post] Available at: https://gilscvblog.wordpress.com/2013/08/18/a-short-introduction-to-descriptors/ [Accessed on 15 June 2015].

Hager, G. and Belhumeur, P., 1998. *Efficient region tracking with parametric models of geometry and illumination*. IEEE Transactions on Pattern Analysis and Machine Intelligence, vol. 20 (10), 1025–1039

Harris, M., 2013. *CUDA Pro Tip: Write Flexible Kernels with Grid-Stride Loops* [online] available at: http://devblogs.nvidia.com/parallelforall/cuda-pro-tip-write-flexible-kernels-grid-stride-loops/ [Accessed on 18 May 2015].

Harris, C. and Stephens, M., 1988. *A combined corner and edge detector* [pdf]. Proceedings of the 4th Alvey Vision Conference, pp.147–151. Available at: http://www.bmva.org/bmvc/1988/avc-88-023.pdf [Accessed 19 June 2015].

Huang, C., Ai, H., Li, Y. and Lao, S., 2007. *High-Performance Rotation Invariant Multiview Face Detection*. [pdf] IEEE Transactions ON PATTERN ANALYSIS AND MACHINE INTELLIGENCE. Available at: http://media.cs.tsinghua.edu.cn/~imagevision/papers/[2007][pami]High%20Performance%20Rotation%20Invariant%20Multi-View%20Face%20Detection%20i0671.pdf [Accessed 30 June 2015].

Huang, C., Ai, H., Li, Y. and Lao, S., 2005*. Vector Boosting for Rotation Invariant Multi-View Face Detection* [pdf] Available at: http://lear.inrialpes.fr/people/triggs/student/vj/huang-iccv05.pdf [Accessed on 30 June 2015].

Impact Research Group, (2015) *Parboil Benchmarks* [online] University of Illinois. Available at: http://impact.crhc.illinois.edu/Parboil/parboil.aspx [Accessed 27 June 2015].

Karimi, K., Dickson, N. G. and Hamze, F., 2010. *A Performance Comparison of CUDA and OpenCL*. [online] Cornell University Library. Available at: http://arxiv.org/abs/1005.2581 [Accessed 24 June 2015].

Komatsu, K., Sato, K., Arai, Y., Koyama, K., Takizawa, H. and Kobayashi, H., 2010. *Evaluating Performance and Portability of OpenCL Programs*. [pdf] The Fifth International Workshop on Automatic Performance Tuning. Available at: http://citeseerx.ist.psu.edu/viewdoc/download?doi=10.1.1.456.5743&rep=rep1&type=pdf [Accessed 24 June 2015].

Li, H., Lin, Z., Shen, X., Brandt, J. and Hua, G., 2015. A Convolutional Neural Network Cascade for Face Detection. [pdf] Available at: http://personal.stevens.edu/~hli18/papers/CVPR2015_CasCNN.pdf [Accessed on 17 January 2016].

Lowe, D. G., 1999. *Object Recognition from Local Scale-Invariant Features*. [pdf] Available at: http://www.cs.ubc.ca/~lowe/papers/iccv99.pdf [Accessed on 15 October 2015].

Lowe, D. G., 2004. *Distinctive Image Features from Scale-Invariant Keypoints*. International Journal of Computer Vision 60(2) pp.91-110.

Lucas, B. and Kanade, T., 1981. *An iterative image registration technique with an application to stereo vision*. [pdf] Stanford. Available at: http://graphics.stanford.edu/courses/cs448a-00fall/lucaskanade81.pdf [Accessed on 11 November 2015].

Lucey, S., Wang, Y., Cox, M., Sridharan, S. and Cohna, J. F., 2009. *Efficient Constrained Local Model Fitting for Non-Rigid Face Alignment* [online] NCBI. Available at: http://www.ncbi.nlm.nih.gov/pmc/articles/PMC2799037/ [Accessed on 27 December 2015].

Luitjens, J., 2014. *Faster Parallel Reductions on Kepler* [online] NVIDIA. Available at: http://devblogs.nvidia.com/parallelforall/faster-parallel-reductions-kepler/ [Accessed on 10 October 2015].

Mathias, M., Benenson, R., Pedersoli, M. and Van Gool, L., 2014. *Face detection without bells and whistles*. ECCV. 8692, pp.720-735.

Matthews, I. and Baker, S., 2004. *Active appearance models revisited*. IJCV, 60(2), pp.135–164.

NVIDIA, 2012. *NVIDIA's Next Generation CUDA™ Compute Architecture: Kepler™ GK110, Whitepaper*. [pdf] NVIDIA. Available at: http://www.nvidia.co.uk/content/PDF/kepler/NVIDIA-Kepler-GK110-Architecture-Whitepaper.pdf [Accessed 20 November 2015].

NVIDIA, 2016. CUDA Toolkit Archive. [online] NVIDIA Available at: https://developer.nvidia.com/cuda-toolkit-archive [Accessed 8 January 2016].

NVIDIA developer zone, 2015. *CUDA toolkit documentation*. [online] NVIDIA. Available at: http://docs.nvidia.com/cuda/cuda-c-programming-guide/#axzz3eAOkWhLD [Accessed 20 June 2015].

PASCAL, 2005. *The Pascal object recognition database collection*. [online] University of Southampton. Available at: http://www.pascalnetwork.org/challenges/VOC/ [Accessed 20 June 2015].

Ranjan, R., Patel, V. M. and Chellappa, R., 2015. *A Deep Pyramid Deformable Part Model for Face Detection*. [pdf] Cornell University Library. Available at: http://arxiv.org/pdf/1508.04389v1.pdf [Accessed on 17 January 2016].

Saragih, J., Lucey, S. and Cohn, J., 2011. *Deformable model fitting by regularized landmark mean-shift*. IJCV, 91(2), pp.200-215.

Shen, X., Lin, Z., Brandt, J. and Wuk, Y., 2013. *Detecting and aligning faces in image retrieval.* CVPR, pp.3460-3467.

Tzimiropoulos, G., 2015*. Project-Out Cascaded Regression with an application to Face Alignment.* CVPR, pp.3659-3667.

Viola, P. and Jones, M. J., 2003. *Fast Multi-view Face Detection* [pdf] Available at: http://citeseerx.ist.psu.edu/viewdoc/download?doi=10.1.1.145.7598&rep=rep1&type=pdf [Accessed 1 July 2015].

Viola, P. and Jones, M. J., 2004. *Robust Real-Time Face Detection*. [pdf] International Journal of Computer Vision. Available at: http://www.vision.caltech.edu/html-files/EE148-2005-Spring/pprs/viola04ijcv.pdf [Accessed 29 June 2015].

Wales Online, 2015. *Selfies and a pint as Barbarians squad get together* [image online] Available at: http://www.walesonline.co.uk/sport/rugby/rugby-news/wales-internationals-adam-jones-alex-9332896 [Accessed on 10 January 2016].

Wang, N., Gao, X., Tao, D. and Li, X., 2014. *Facial Feature Point Detection: A Comprehensive Survey* [pdf] Available at: http://arxiv.org/pdf/1410.1037.pdf [Accessed on 24 December 2015].

Yan, J., Zhang, X., Lei, Z. and Li, S., 2013. *Face detection by structural models. Image and Vision Computing*. 32(10), pp.790-799.

Yang, S., Luo, P., Loy, C.C. and Tang, X., 2015. *From Facial Parts Responses to Face Detection: A Deep Learning Approach*. [pdf] Cornell University Library. Available at: http://arxiv.org/pdf/1509.06451v1.pdf [Accessed on 17 January 2016].

Zhu, X. and Ramanan, D., 2012. *Face detection, pose estimation, and landmark estimation in the wild*. CVPR, pp.2879–2886.

10 Appendix A

There are two main API's that can be used to program the GPU, they are CUDA by NVIDIA and the open computer language (OpenCL) which is owned by Apple and managed by the Khronos group. Khronos (2015) state that "OpenCL™ is the first open, royalty-free standard for cross-platform, parallel programming of modern processors found in personal computers, servers and handheld/embedded devices." This means that OpenCL can not only be used on GPU's by NVIDIA and AMD, it can also be used on all multi-core CPU's, mobile GPU's and Cell Broadband Engine (BE) processors. Whereas CUDA will only work on GPU's that are made by NVIDIA, a complete list of GPU's that CUDA is compatible with can be found at https://developer.NVIDIA.com/cuda-gpus.

GPU Supplier	Market share this quarter	Market share last quarter	Market share last year
AMD	22.5%	24.0%	35.0%
Matrox	0.00%	0.10%	0.10%
NVIDIA	77.5%	76.0%	64.9%
S3	0.00%	0.00%	0.00%
Total	100%	100%	100%

Table 10.1: Discrete graphics chip market share 2015 (Source: Jon Peddie Research, 2015)

If we compare the market for discrete GPU's for desktop personal computers, Table 10.1. We can see that according to analysts from Jon Peddie Research (2015) who are an industry research and consulting firm for graphics and multimedia, that the dominate vendor is NVIDIA with a market share of 77.5%. It can also be seen that the market share of AMD is in decline.

Although OpenCL can run on a variety of GPU's and CPU's that are manufactured by different vendors, they all require a variety of different optimisations and extensions to fully support their different architectural features in order to maximise performance. Therefore, porting OpenCL code from one vendor to another is not a straight forward task.

10.1 CUDA and OpenCL Performance comparison

A fair comparison between CUDA and OpenCL can only be achieved on an NVIDIA graphics card as CUDA is not compatible with any other vendor. But, this is not currently possible, as NVIDIA has not implemented OpenCL 2.0 into their driver set. It was reported by AnandTech (2015) that NVIDIA have only just recently added support for OpenCL 1.2 into their driver release, version 350.05 on April 2015. Therefore, this thesis will summarise the results of recent performance comparisons from peer reviewed published papers.

Research undertaken by (Karimi et al, 2010) into the performance comparison between CUDA and OpenCL in data transfer to and from the GPU, kernel execution and end-to-end application running times, was done by implementing a Monte Carlo simulation of a quantum spin system with quantum bit (qubits) sizes ranging from 8 to 128. This was accomplished using an NVIDIA GeForce GTX-260 GPU. To profile the application, they split it into six stages

1. Setup GPU
2. Read input
3. Copy data to GPU
4. Execute kernel on the GPU
5. Copy data beck to the host
6. Process returned data on CPU and output results

Table 10.2 summarise of the results that they achieved and is broken down into 3 parts. Kernel Running Time (step 4), Data Transfer Time (steps 3 and 5) and End-To-End Running time (steps 1-6).

Qubits	Kernel Running Time		Data Transfer Time		End-To-End Running Time	
	CUDA	OpenCL	CUDA	OpenCL	CUDA	OpenCL
8	1.96	2.23	0.009	0.011	2.94	4.28
16	3.85	4.73	0.015	0.023	5.39	7.45
32	7.65	9.01	0.025	0.039	10.16	12.84
48	13.68	19.80	0.061	0.086	17.75	26.69
72	25.94	42.17	0.106	0.146	32.77	54.85
96	61.10	71.99	0.215	0.294	76.24	92.97
128	100.76	113.54	0.306	0.417	123.54	142.92

Table 10.2: CUDA and OpenCL GPU kernel execution, data transfer and application running costs. All times are measured in seconds (Source: Karimi et al, 2010).

Although CUDA and OpenCL where both executed with nearly identical code, it can be seen from Table 10.2 that CUDA's kernel execution and data transfer times are consistently faster than OpenCL. They did not give any reasons as to why CUDA performed faster than OpenCL.

Other research by (fang et al, 2011) also performed a comparison between CUDA and OpenCL using 16 different benchmark tests, ranging from synthetic to real-world applications. They ran all their experiments on the NVIDIA GTX280 and GTX480 GPU. For a unified comparison in performance between CUDA and OpenCL they used a normalised performance metric

$$PR = \frac{Performance_{OpenCL}}{Performane_{CUDA}}$$

Where $PR < 1$ then CUDA's performance is considered to be better than OpenCL.

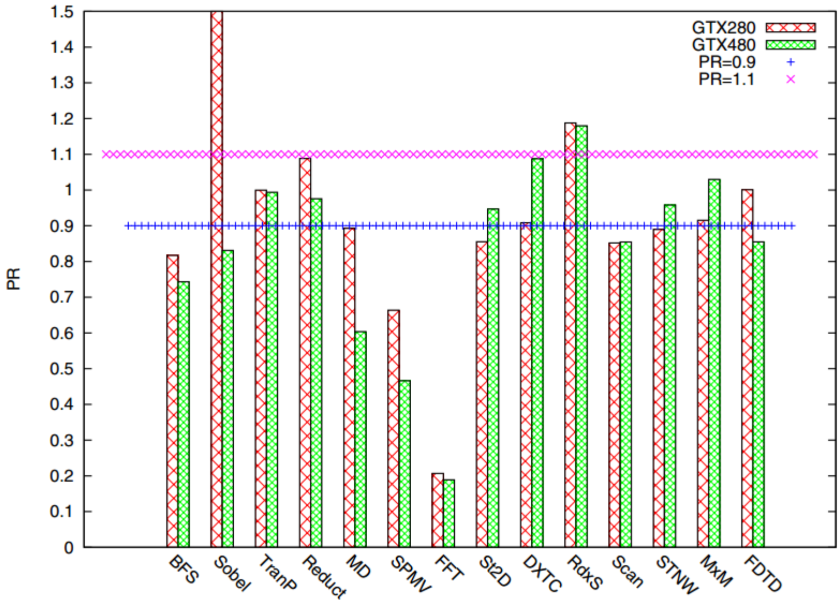

Figure 10.1: Unified performance comparison of selected benchmarks using NVIDIA's GeForce GTX 280 and GTX480. It is assumed that CUDA and OpenCL have a similar performance if the result lies between 0.9 and 1.1 (Source: fang et al, 2011)

As can be seen in Figure 10.1 initial tests show that CUDA performs up to 30% better than OpenCL. With the most notable difference being the fast Fourier transform (FFT) where CUDA's performance was 5 times faster than OpenCL. The reason why CUDA out performed OpenCL according to (fang et al, 2011) is because of the differences between CUDA and OpenCL compilers provided by NVIDIA. They found that the PTX code generated by the CUDA compiler was better optimised. But, after optimising the OpenCL kernels they found that the differences in performance where mostly negligible.

Recent research by (Bernabé et al, 2012), performed a comparison between CUDA and OpenCL by implementing a 3D Fast Wavelet Transform (3D-FWT), this was done using an NVIDIA Tesla™ C2050 GPU, which is based on the Fermi architecture. For their tests they split the algorithm down into 5 stages as can be seen in Table 10.3, and for each stage CUDA performed better than OpenCL. Particularly interesting is the huge difference in the transfer times to and from the GPU, where CUDA performed approximately two to five times faster than OpenCL.

3D-FWT	Frame size					
	512x512		1Kx1K		2Kx2K	
	CUDA	OpenCL	CUDA	OpenCL	CUDA	OpenCL
1. CPU to GPU transfer	11.62	25.19	45.6	86.38	181.63	325.52
2. 1D-FWT on frames	2.11	3.53	4.18	6.64	7.73	11.73
3. 1D-FWT on rows	2.37	3.85	2.39	5.89	2.39	6.97
4. 1D-FWT on cols	2.29	3.80	6.86	9.82	25.15	29.29
5. GPU to CPU transfer	10.82	50.75	41.58	167.66	164.68	637.96

Table 10.3: CUDA and OpenCL execution times for a tiled 3D-FWT implementation on an input video containing 64 frames of increasing sizes. All times are measured in milliseconds. (Source: Bernabé et al, 2012).

The reason for this according to (Bernabé et al, 2012), is because OpenCL has a large environmental setup overhead, and that the huge discrepancy in transfer times is because OpenCL is designed for general compute devices.

Other research conducted by (Komatsu et al, 2010) was done where they selected two programs from the NVIDIA GPU Computing SDK 3.0, a bandwidth test and matrix multiply, plus three CUDA programs from the parboil benchmark suite (The Impact Research Group, 2015), Coulombic Potential (CP), Magnetic Resonance Imaging Q (MRI-Q), and Magnetic Resonance Imaging FHD (MRI-FHD). They ported the CUDA code from these programs to OpenCL as faithfully as possible, by only changing syntax/API calls where needed.

In their initial tests using a NVIDIA Tesla C1060 GPU. Figure 10.2, showed that CUDA ran all the algorithms several times faster than OpenCL, with the exception of the bandwidth test which was near identical in speed.

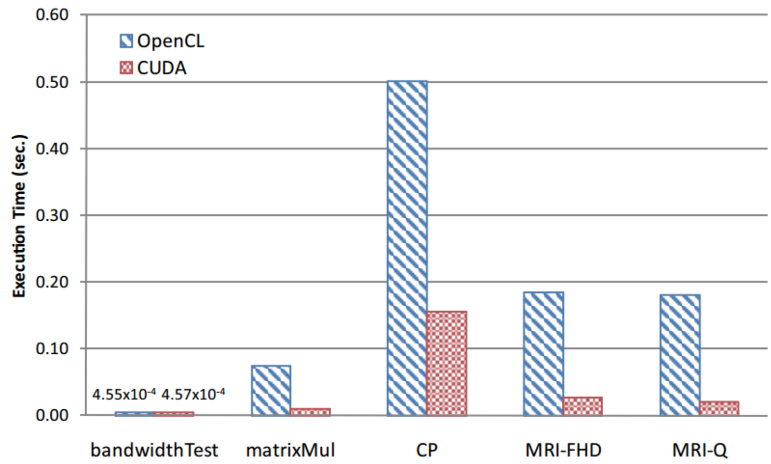

Figure 10.2: Initial benchmarks for CUDA and OpenCL, running near identical kernel code on an NVIDIA Tesla C1060 GPU. (Source: Komatsu et al. 2010)

The reason why the bandwidth test was nearly identical is because only API calls where invoked to transfer data. Therefore, they suggested that the cost in invoking API calls in OpenCL is almost the same as for invoking them in CUDA.

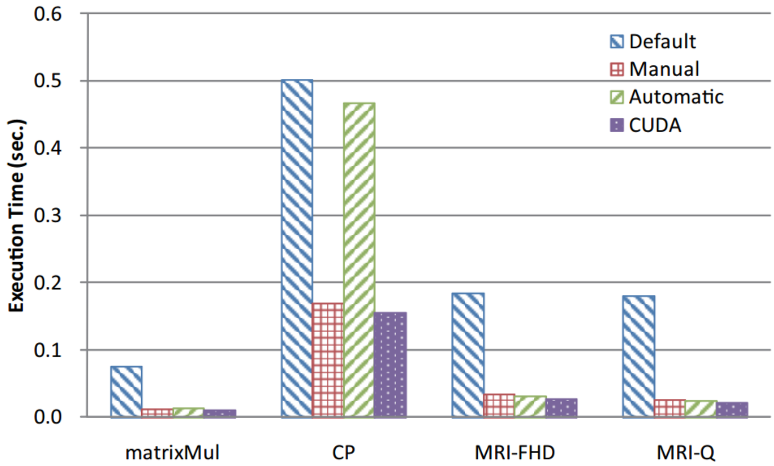

Figure 10.3: Performance of benchmarks after applying manual optimisations. (Source: Komatsu et al. 2010)

They then investigated two ways to increase the speed of OpenCL, first they manually optimised the PTX code that was generated by the OpenCL compiler, and secondly they applied automatic optimisations to the compiler by enabling the "*-cl-fast-relaxed-math"* option. The results of which can be seen in Figure 10.3. Which shows with the exception of CP the results are close, with CUDA been slightly faster.

The reason according to (Komatsu et al, 2010) as to why the CP algorithm performs so badly in the automatically optimised compiler is because the intrinsic instruction "*rsqrt"* was not utilised. They conclude that the perceived differences in performance is caused by the optimisation capabilities of the compilers.

As OpenCL can be used on multiple GPU's (Komatsu et al, 2010) also compared an AMD Radeon HD 5870 against the NVIDIA Tesla C1060 using the same tests as before. They concluded that although OpenCL works on various GPUs/CPU's the code for each device will need to be further optimised to achieve maximum performance.

10.2 Conclusion

Although OpenCL has stronger cross platform support, and is nearly identical in performance compared to CUDA. In this thesis the preferred API that is to be used to implement the proposed system is CUDA. The reasons for this decision are because, (1) CUDA's development and profiling tool sets are far more mature compared to OpenCL's, (2) with the release of CUDA 7.0 the C++11 standard is fully supported by the nvcc compiler, (3) stronger documentation and on-line support, (4) NVIDIA currently dominate the market for desktop PCs.